Computers & Geosciences 146 (2021) 104610

Contents lists available at ScienceDirect

Computers and Geosciences

journal homepage: www.elsevier.com/locate/cageo

Review article

Sensitivity of glacier elevation analysis and numerical modeling to CryoSat-2 SIRAL retracking techniques

Thomas Trantow[a,*], Ute C. Herzfeld[a,b], Veit Helm[c], Johan Nilsson[d]

[a] Department of Electrical, Energy and Computer Engineering, University of Colorado, Boulder, CO, USA
[b] Cooperative Institute for Research in Environmental Sciences, University of Colorado, Boulder, CO, USA
[c] Glaciology Section, Alfred Wegener Institute, Helmholtz Centre for Polar and Marine Research, Bremerhaven, Germany
[d] NASA Jet Propulsion Laboratory, 329C–Sea Level and Ice, California Institute of Technology, Pasadena, CA, 91109-8099, USA

ARTICLE INFO

Keywords:
Crevasse modeling
CryoSat-2
Radar altimetry
Bering glacier
Retracking methods
Glacier topography

ABSTRACT

The CryoSat-2 radar altimetry mission, launched in 2010, provides key measurements of Earth's cryosphere. CryoSat-2's primary instrument, the Synthetic Aperture Interferometric Radar Altimeter (SIRAL), allows accurate height measurements of sloped ice-surfaces including the highly crevassed Bering-Bagley Glacier System (BBGS) in southeast Alaska. The recent surge of the BBGS in 2011–2013, which resulted in large-scale elevation changes and wide-spread crevassing, presents an interesting challenge to the processing of the SIRAL measurements. Derivation of surface height is achieved by retracking the received waveform of the altimeter signal. Several such retracking methods have been developed. In this paper, we investigate the influence of six unique SIRAL retracking methods on (1) Digital Elevation Model (DEM) generation, (2) analysis of ice-surface topography, and (3) numerical modeling results of the BBGS during surge. First, we derive a surface DEM for each retracked dataset using kriging. The swath-processed dataset provides 100–250 times more points than the other datasets, which decreases DEM uncertainty associated with data coverage by a factor of 2–4. Differences between the six resulting DEMs imply that retracking methods can have significant effects on elevation and elevation-change analysis, but we find that lower-level processing has larger effects. Next, the sensitivity of the data-model connection is evaluated using a finite element model of the BBGS surge. We set up six modeling experiments, each initiated with a unique input surface DEM derived from the various retracking methods. While retracking choices effect estimation of unknown model parameters related to crevasse simulation, we have developed a procedure to limit these effects resulting in remarkably consistent parameter optimization across modeling experiments. Each model experiment yields an optimal friction coefficient in the sliding law of $10^{-5}\ \frac{MPa\cdot a}{m}$, while estimates of the optimal von Mises stress threshold for crevasse initiation ranged between 230 and 240 kPa.

1. Introduction

1.1. Study in a broader context

Both collection of Earth observation data and modeling of physical processes have seen great advances in recent years, accelerating from previous decades. Increasingly large and detailed Earth observation data sets are becoming available for scientific investigations, with current satellite missions collecting terabytes of data per day, e.g., NASA's ICESat-2 (Markus et al., 2017; Neumann et al., 2019) and ESA's Sentinel series (Berger et al., 2012). At the same time, modeling of the Earth system has reached much higher standards in recent years than ever before (Bentsen et al., 2012; Jungclaus et al., 2013; Voldoire et al., 2013; Kay et al., 2015; Sokolov et al., 2018). This includes increased model resolution, expanded and integrated physical process modeling, and the limiting of uncertainties in projection models through intercomparison projects (e.g. Bindschadler et al. (2013); Nowicki et al. (2013a, Nowicki et al., 2013, 2016)). As a result, a new challenge emerged in linking observational data and models.

Cryospheric height observations with sufficient spatiotemporal coverage require measurements from satellites, which since the 1980s has come in the form of radar altimeter measurements (Brenner et al., 1983; Zwally et al., 1983). The processing of radar altimeter data has been the focus of a number of influential studies, from Davis (1993) for

---

* Corresponding author.
E-mail address: trantow@colorado.edu (T. Trantow).

https://doi.org/10.1016/j.cageo.2020.104610
Received 5 December 2019; Received in revised form 8 September 2020; Accepted 17 September 2020
Available online 4 October 2020

early spaceborne radars, to Helm et al. (2014) and Nilsson et al. (2016) for the cutting-edge radar measurements made by the CryoSat-2 satellite (Wingham et al., 2006).

In order to understand the physical processes involved in glacial change, and to predict future evolution of Earth's ice-masses, numerical models of ice evolution are required. There are currently several leading ice sheet models investigating glacial response to climatic changes, including the Community Ice Sheet Model (CISM) (Price et al., 2011; Lipscomb et al., 2019), the SImulation COde for POLythermal Ice Sheets (SICOPOLIS) (Greve et al., 2011), the Ice Sheet System Model (ISSM) (Larour et al., 2012), the Parallel Ice Sheet Model (PISM) (Winkelmann et al., 2011), and an Elmer/Ice model (Gagliardini et al., 2013). These models, along with several others, have been compared and evaluated in community-wide comparison studies such as SeaRISE (Sea-level Response to Ice Sheet Evolution) (Bindschadler et al., 2013; Nowicki et al., 2013a, Nowicki et al., 2013) and ISMIP6 (Ice Sheet Model Intercomparison Project) (Nowicki et al., 2016; Goelzer et al., 2020; Seroussi et al., 2020). Inter-model comparison methods often lack spatial information, with ice sheet-wide results boiled down to a single point in a time series analysis, and visualized in a simple 2D line plot (e.g. Bindschadler et al. (2013)). However, comparison methods exist, such as the Map Comparison Method (MAPCOMP) (Herzfeld and Merriam, 1990), that provide spatial maps of similarities and dissimilarities among input maps, i.e., ice sheet-wide model results, rather than providing a single number quantifying correlation.

There are several approaches that employ observational data to improve numerical modeling (e.g., Herzfeld et al. (2015)), and are often in the form of data assimilation (e.g., Goldberg and Sergienko (2011); Brinkerhoff and Johnson (2013); Larour et al. (2014)). However, many of these studies are performed independently from the analysis and processing of the assimilated data and often assume they are using the best available observations to constrain their models. It is therefore rare to find analyses that combine data processing, data analysis, modeling results and model parameterization all in a single study, where doing so could help identify important outstanding uncertainties in cryospheric investigation.

This paper serves as both a review of the current model-data connection techniques in cryospheric science, and each component therein, and a presentation of a novel sensitivity analysis that combines glaciological methods of observation, numerical modeling and model-data connection into a single study. In particular, our sensitivity analysis provides links between radar altimetry, satellite observations, altimeter data processing, numerical modeling of ice dynamics and crevasses, inter-model comparison and model-data connection. Following a review of state-of-the-art methods and approaches in each of the observation, analysis and modeling fields, we present our new study that combines each of these aspects for investigation of the effects that data processing have on glacier elevation analysis, numerical modeling results and the subsequent interpretations. This is the first study to investigate the effect that altimeter data processing has on numerical modeling of glacier dynamics.

1.2. Introduction to the sensitivity study

On April 8th, 2010, the European Space Agency (ESA) launched the CryoSat-2 satellite with the objective of continuously monitoring land- and sea-ice to investigate the connection between the melting ice and sea level rise and its contribution to climate change (Wingham et al., 2006). CryoSat-2's Synthetic Aperture Interferometric Radar Altimeter (SIRAL) continues to supply height measurements of the cryosphere through 2020. However, there exist a variety of level-2 processing, or retracking, techniques to derive elevation estimations of ice surfaces, each yielding unique datasets despite starting with the same raw SIRAL measurement (e.g., Bouffard (2015); Bouffard et al. (2017); Helm et al. (2014); Nilsson et al. (2016); Gray et al. (2015, 2017)).

In our previous studies of the 2011–2013 surge of the Bering-Bagley Glacier System (BBGS), Alaska, we have utilized the available CryoSat-2 elevation estimates provided by ESA (Trantow and Herzfeld, 2016, 2018). Having shown that CryoSat-2 measurements are useful in investigating large mountain glaciers, even during large elevation changes typical of a surge, Trantow and Herzfeld (2016) proceeded to derive a time series of ice-surface Digital Elevation Models (DEMs) to interpret surge progression in the glacier system from 2011 to 2013. This study used the data given by the processing and retracking techniques of ESA's Baseline-B level-2 product (Bouffard, 2015). In Trantow and Herzfeld (2018), we created an ice-surface DEM for input into an ice-dynamic numerical-model of the BBGS that simulated observed crevasses during the major surge phase in early 2011. The DEM for this study was derived using data from ESA's updated Baseline-C level-2 product (Bouffard et al., 2017). We observed large differences between the Baseline-B and Baseline-C elevation datasets for the BBGS whose highly crevassed surface, set in a mountainous region, provides a difficult challenge in the processing of CryoSat-2 SIRAL measurements.

In the analysis of present paper, we seek to quantify the sensitivity of higher level data analysis for the BBGS, such as DEM generation, elevation-change interpretation and modeling results, to differences in surface elevation estimates provided by various CryoSat-2 retracking techniques. We investigate not only ESA's standard products (versions Baseline-B and Baseline-C), but also height estimates provided by the Threshold First Maximum Retracking Algorithm (TFMRA) outlined in Helm et al. (2014), and the Leading-edge Maximum Gradient (LMG) retracker (Nilsson et al., 2016). We begin by presenting a review of the relevant background information on radar altimetry, CryoSat-2 and glacier surging in Section 2. Section 3 provides an introduction to the various CryoSat-2 processing techniques used in our study along with a description of the resulting datasets for the BBGS. This section also provides a brief overview of the techniques used in DEM generation, numerical modeling, crevasse-based model-data comparisons and the model sensitivity analysis. Finally, Section 4 presents the results of the sensitivity study which is discussed with regards to effects that different CryoSat-2 processing techniques have on error estimates in DEM generation, estimation of unknown model parameters, and the overall match of modeled results to observations.

2. Background

2.1. Radar altimetry

Satellite radar altimetry has been used to investigate topography and elevation change in the cryosphere since the 1980s (Brenner et al., 1983; Zwally et al., 1983). Early satellite radar altimeter missions aimed at investigating surface characteristics of the ocean, such as sea level and wind patterns, and difficulties arose when measuring ice surfaces due to topographic features, surface slopes, and volume penetration of the radar wave into the snow/firn (Rémy and Parouty, 2009). These cryospheric challenges in early satellite altimeter missions were overcome through development of new surface scattering models and retracking methods (e.g., Davis (1993); Bamber (1994); Davis (1997)). In addition, Herzfeld et al. (1993) applied advanced kriging methods to overcome the problem of estimating ice-surface topography from radar-altimeter data over sloping glaciers, utilizing the geometry of the satellite ground tracks. This method is used to derive elevation maps in the Atlas of Antarctica (Herzfeld, 2004).

Accuracy and spatio-temporal coverage in satellite altimetry improved dramatically with the launch of ESA's ERS-1 satellite in 1991. ERS-1 altimeter measurements in the cryosphere allowed the derivation of ice-sheet wide DEMs of the ice surface topography (Bamber and Huybrechts, 1996). These DEMs serve as important boundary conditions for numerical models aimed at predicting ice sheet evolution and cryospheric contributions to sea-level rise (Marsiat and Bamber, 1997). There are however, many methods of processing raw radar altimeter measurements and a variety of interpolation schemes that researchers employ to derive ice-surface DEMs. Therefore, given the same initial measurement, DEMs can differ significantly when given as boundary conditions to a numerical model resulting in dissimilar simulations (e.g., Marsiat and Bamber (1997); Bamber and Gomez-Dans (2005)). Marsiat and Bamber (1997) show that differences in ERS-1 processing methods have substantial influence on numerical simulations of Antarctica's climate. However, it was limitations of the ERS instrument itself, rather than differences in the processing chain, that resulted in the largest uncertainties in cryospheric applications, which motivated the development of a satellite radar altimeter whose main objective was measuring ice-covered regions.

To this end, ESA designed the CryoSat-2 satellite altimetry mission to provide continuous synoptic measurements of Earth's land and marine ice fluxes (Wingham et al., 2006). CryoSat-2's primary instrument, the SIRAL altimeter, operates in three modes including Synthetic Aperture Radar Interferometric (SARIn) mode that employs two receiver antennas for operation in sloped areas such as those along the margins of the ice sheet or in mountainous regions. In this mode, SIRAL utilizes the SAR principle to increase the spatial resolution of radar altimeter data compared to operation as a conventional pulse limited radar system in low-resolution mode (LRM). The measurement accuracy of cryospheric targets provided by CryoSat-2, along with its high spatio-temporal coverage up to ±88° latitude, allows the derivation of ice sheet-wide surface DEMs (e.g., Helm et al. (2014); Nilsson et al. (2016); Fei et al. (2017); Slater et al. (2018)), with uncertainties less than 3 m±15 m in the case of Helm et al. (2014).

Even though initial CryoSat-2 measurements have been successful in measuring the cryosphere, there are still open problems in the standard processing chain leading to the level-2 product produced by ESA (Wingham et al., 2006; ESA, 2014; Helm et al., 2014; Mannan, 2017), which is the main product for the standard CryoSat-2 user. This has motivated the derivation of alternate methods of level-2 processing of CryoSat-2 measurements, such as the TFMRA (Helm et al., 2014) or LMG (Nilsson et al., 2016) methods, which are investigated in this paper with regards to their effect on analysis of the surging BBGS.

2.2. Glacier surging and crevasses

A glacier surge is a quasi-periodic episode of rapid acceleration, which interrupts a glacier's quiescent phase of normal flow. Surge glaciers are restricted to certain geographical region including Alaska, Svalbard, Iceland, the Karakoram Mountains and the margins of the Greenland and Antarctic ice sheets (Meier and Post, 1969; Dolgushin and Osipova, 1975; Herzfeld, 1998; Jiskoot et al., 2001). Surging is a type of *glacial acceleration*, and is the least understood type due to a relative paucity of observations (Meier and Post, 1969; Fowler, 1987; Raymond, 1987; Murray et al., 2003). Other types of glacial acceleration include always-fast-flowing ice streams, ice streams with a state-switching behavior, and tidewater glaciers with long periods of velocity changes (Clarke, 1987; Truffer and Echelmeyer, 2003). Glacial acceleration has been identified as one of the main uncertainties in estimating future global sea-level rise through numerical modeling (Stocker et al., 2013). Before the different types of glacial acceleration can be included in ice-sheet-scale models, particularly surging, the unknown physical mechanisms controlling the surge phenomenon must be identified and represented in a dedicated surge model at the scale of a single glacier system. For this reason, we have created a numerical surge model of the Bering Bagley Glacier System (BBGS), Alaska (Trantow and Herzfeld, 2018) (Fig. 1), using the finite element software Elmer/Ice (Gagliardini et al., 2013). The recent surge of the BBGS in 2011–2013 provides a rare opportunity to investigate a surge in a large and complex glacier system similar to those found in the margins of the major ice sheets. A complex surge-glacier system consists of both surging and non-surging parts, where surge initiation and progression effects different locations at different times. Of particular interest is the early-2011 phase of the recent surge, where the largest surge effects were observed during the initial rapid acceleration in lower and central Bering Glacier (Herzfeld et al., 2013b; Trantow and Herzfeld, 2018). The analysis in the present paper focuses on this surge phase.

Cumulating airborne and satellite observations, numerical modeling and model-data comparison allows thorough investigation of this BBGS surge (Herzfeld et al., 2013a, b; Trantow and Herzfeld, 2016, 2018). These previous studies have taken an approach centered on the most conspicuous manifestation of surging: crevasses. Using crevasses as the

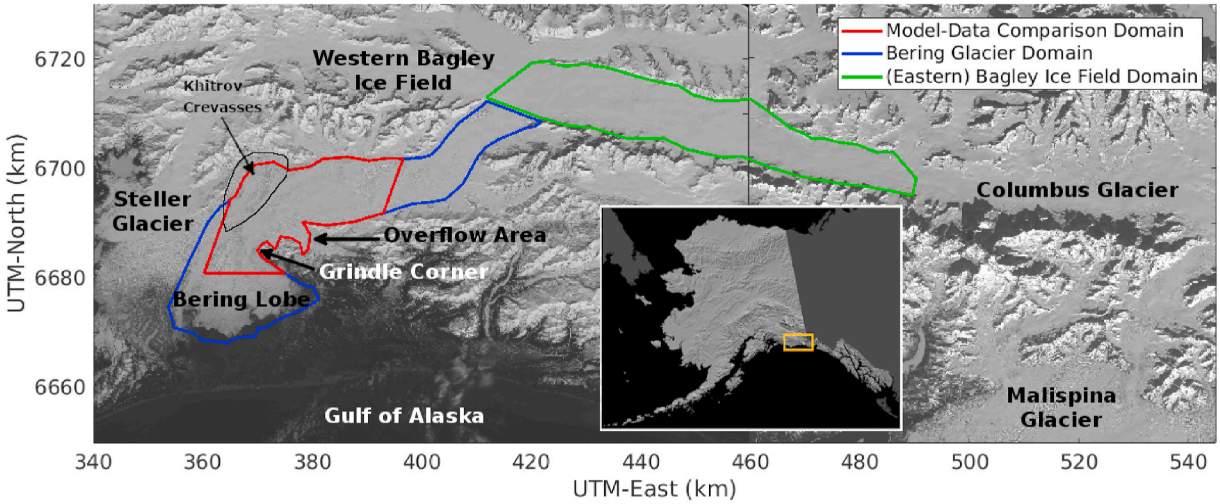

Fig. 1. The Bering-Bagley Glacier System and the surrounding area with analysis domains. Labeled are important features of the BBGS and some of the major nearby glaciers in southeast Alaska. The Bering Glacier domain is outlined in blue while the (Eastern) Bagley Ice Field portion of the BBGS is outlined in green. The combination of the displayed Bering Glacier and Bagley Ice Field domains constitute the horizontal extent of the BBGS numerical model domain. The red line outlines the domain of analysis for the crevasse-based model-data comparison techniques employed in this paper, which is the intersection of the BBGS model domain and the image analysis domain from the April 15, 2011 Landsat-7 image. The Khitrov crevasse field, lying within the black ellipse just below the Khitrov Hills, is a location of large surge crevasses that opened up during the early-2011 phase of the recent surge. Map coordinates: Universal Transverse Mercator (UTM), zone 7. Background image: Landsat-8 panchromatic acquired April 28, 2013 (left) and Landsat-8 panchromatic acquired March 7, 2014 (right). Alaskan reference image: U.S. Geological Survey Map I-2585.

basis of analysis has the advantage of requiring only a single observation to derive comprehensive geophysical information. Traditional glaciological analysis often relies upon velocity data to connect models to observations. However, velocity derivation requires the correlation of two separate observations, separated in time, which often yield sparse and unreliable estimates during rapid ice-deformation (see for example, Fatland and Lingle (1998); Burgess et al. (2013)). Therefore, these previous crevasse-based studies on the BBGS surge have made significant methodological contributions to the study of fast-moving ice. The present paper also contributes to our understanding of BBGS surges, and glacial acceleration in general, by quantifying uncertainties in the elevation and elevation-change analysis of Trantow and Herzfeld (2016) and the modeling results of Trantow and Herzfeld (2018) introduced by the choice of the CryoSat-2 level-2 (retracked) product.

3. Methods

3.1. Data and retracking methods

Radar altimeter measurements consist of transmitting a pulse in the nadir direction and measuring the backscattered energy. The returned signal is available as discretized power with respect to time providing an altimeter "waveform". Post-processing of the return waveform signal is required since the leading edge deviates from the satellite's on-board tracking gate leading to errors in range to the surface and thus, elevation retrieval. The range correction is termed "retracking". Several retracking algorithms exist for each satellite altimeter, each with their own advantages and disadvantages, which can lead to significant differences in elevation estimation (Davis, 1997; Bamber and Gomez-Dans, 2005). In this study, we investigate analysis sensitivity to six different BBGS elevation datasets, each derived from a different retracking method applied to the same raw CryoSat-2 SARIn measurements. Each retracked dataset consists of CryoSat-2 data acquired between November 2010 to April 2011, from which a DEM is constructed to represent the BBGS ice-surface in early-2011 when the major surge phase occurred. The surge-induced effects during this time period, consisting of wide-spread crevassing and large-scale elevation changes, occurred mainly within our model-data comparison domain (red in Fig. 1) (Trantow and Herzfeld, 2018).

The first two datasets we test are a result of the standard level-2

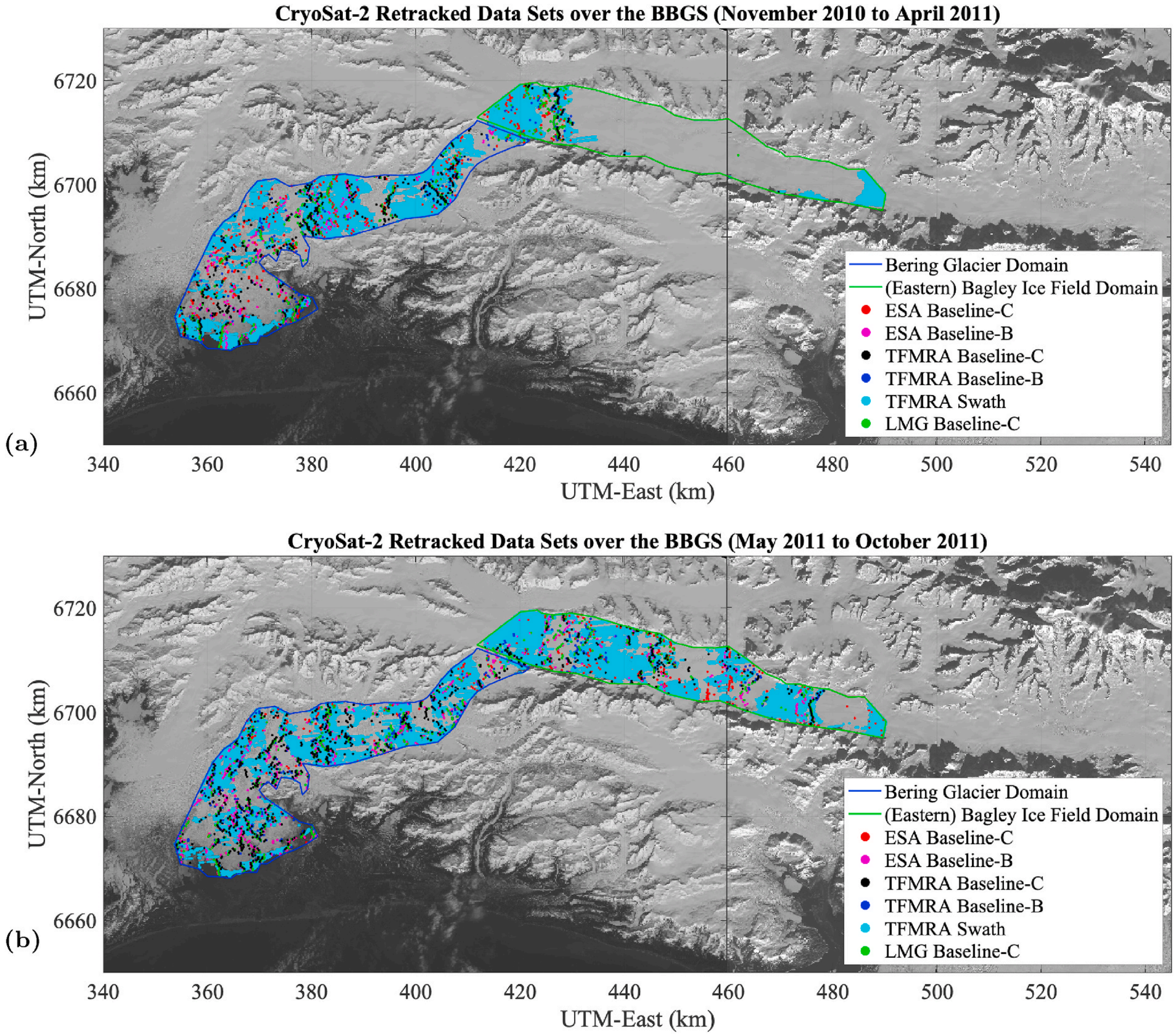

Fig. 2. Coverage of the CryoSat-2 SARIn retracked datasets for the BBGS. (a) Six-month datasets collected between November 2010 and April 2011 (Winter 2010/2011). (b) Six-month datasets collected between May 2011 and October 2011 (Summer 2011). Red and magenta points give elevation estimate locations from ESA's standard level-2 product for Baseline-B and Baseline-C respectively. Black, blue and cyan points show elevation estimates from the TFMRA retracker for Baseline-C, Baseline-B and swath-processing (Baseline-C) respectively. Finally, the green points give elevation estimates from the LMG retracking method applied to the Baseline-C processing chain. The *raddev* filter was applied to each dataset visualized above. (For interpretation of the references to color in this figure legend, the reader is referred to the Web version of this article.)

processing chain from ESA that were available to the public at the time of their release. In particular we use the level-2 Baseline-B data (ESA Baseline-B), released in January 2012, and Baseline-C data (ESA Baseline-C), released in April 2015, whose spatial coverages of the BBGS for the six-month period from November 2010 to April 2011 are seen in Fig. 2 in magenta and red respectively. The description of the core SARIn mode level-2 processing employed by ESA is given in Wingham et al. (2006). The main differences between Baseline-B and Baseline-C level-2 processing is found in Bouffard (2015) and Bouffard et al. (2017).

It is important to note that all Baseline-C data on Bering Glacier contain a 59.959 m elevation bias (Trantow and Herzfeld, 2018). This artifact stems from a compensation issue in the window delay in the processing chain near in-land areas (Mannan, 2017). The issue is under investigation by ESA and is planned to be corrected in the Baseline-D release. In the mean time, we add 59.959 m to each Baseline-C data point on Bering Glacier before any analysis is done.

Next, we investigate three additional datasets in this study that use the TFMRA retracking method. A full description of the processing method is found in Helm et al. (2014). The first TFMRA dataset is derived from ESA's level-1b (L1b) Baseline-B data product (TFMRA Baseline-B), given in blue in Fig. 2, while the second is based on ESA's L1b Baseline-C product (TFMRA Baseline-C), given in black in Fig. 2. The third TFMRA dataset is comprised of *swath processed* data that follows the method introduced by Gray et al. (2013) applied to the standard L1b Baseline-C product (TFMRA Swath Baseline-C). Swath processing is a method that yields multiple height estimates per across-track swath as opposed to a single estimate at the Point of Closest Approach (POCA) serving to increase the spatial coverage of the altimeter data product. The return signal from POCA, that is, the return energy from the location on the ice surface closest to the satellite, is the only unambiguous return energy for geolocation in the across-track swath if the surface slope is less than half of the antenna's angular beamwidth. For low slopes, returns from both sides of POCA will arrive at the receiving antennas simultaneously following the initial POCA signal thereby complicating geolocation for additional across-track elevation estimations. However, under ideally sloped conditions of the glacier surface, additional across-track elevation estimates can be determined within the antenna pattern (Gray et al., 2013; Foresta et al., 2016; Gourmelen et al., 2018). Fortunately, the BBGS has a surface geometry that allows swath-processing at most locations as seen in cyan in Fig. 2.

The final CryoSat-2 dataset is derived using LMG retracking method (Nilsson et al., 2016), which uses ESA's L1b Baseline-C data as input (LMG Baseline-C), given as green in Fig. 2. Concise descriptions of each of the retracking methods introduced so far, excluding the swath processing method, can be found in Sørensen et al. (2018) who investigate the accuracy of these and other retracking methods through comparisons with airborne lidar data over the Austfonna ice cap in Svalbard.

The TFMRA and LMG datasets were not able to employ an ambiguity DEM to improve interferometric processing results due to the unavailability of reliable DEMs of the BBGS during its surge (aside from those derived from CryoSat-2 itself (Trantow and Herzfeld, 2016)). The ambiguity DEMs used in ESA's Baseline-B are known to be inaccurate over steep slopes and are therefore unreliable in correcting for phase-wrapping ambiguities at these locations (Bouffard et al., 2017). In the Baseline-C processing, the DEMs are improved over the Greenland and Antarctic ice sheets, but not Alaska. The future Baseline-D data product aims to improve all land-ice ambiguity DEMs (Bouffard et al., 2017). Since phased-wrapped data points may exist in our datasets, we apply an additional filter based on the calculated experimental variogram for each dataset to remove large outliers (Trantow and Herzfeld, 2016). Termed the Radial-Deviation filter, or *raddev* filter, this algorithm removes most of the data points identified to have been affected by unwrapping errors within each dataset. While a few affected data points may still exist within each dataset, the geostatistical analysis that follows is robust to a relatively small number of outlier points (Herzfeld, 2008). The amount of data points in each dataset before and after the *raddev* filter is applied is given in Table 1.

Final datasets used to construct the ice-surface DEMs consist of valid measurements, identified by application of the *raddev* filter to each retracked dataset, collected between November 1, 2010 and April 30, 2011 (Winter 2010/2011). Six months of CryoSat-2 data provides adequate spatial coverage over Bering Glacier to allow reliable DEM creation (Trantow and Herzfeld, 2016). However, there are little to no valid measurements in the Bagley Ice Field (BIF) during the winter season (November through April), as seen in Fig. 2 and Table 1. Since our analysis of the numerical modeling results focuses on lower and central Bering Glacier, over 25 km downglacier of the BIF, where the dominant surge effects took place in early 2011 (Herzfeld et al., 2013b; Trantow and Herzfeld, 2018), our short-term (≤100 days) simulation results are not dependent on the surface topography in the BIF. Yet, surface topography of the BIF is still needed to run the BBGS model. Data collected during the summer months (May through October) yield sufficient coverage in the BIF due to the different surface conditions. Therefore we include measurements of the BIF from May 2011 through October 2011 from each respective retracking method in each of the winter datasets. This addition allows for surface DEM generation for the entire BBGS, while the sensitivity analysis in this study is restricted to Bering Glacier for Winter 2010/2011 only.

In the following subsections we give a brief overview of the methods of DEM generation and error analysis, ice-dynamic modeling during a surge, crevasse characterization analysis via modeling and image analysis, and crevassed-based model-data comparisons, which are covered in more depth in Trantow and Herzfeld (2016) and Trantow and Herzfeld (2018). We then introduce the methods unique to this paper for testing the BBGS model's sensitivity to input surface topography when simulating crevasses.

3.2. DEM generation

Ice-surface DEMs and associated error measures in this analysis are generated following the geostatistical approach thoroughly described in Trantow and Herzfeld (2016), which was originally developed in a series of studies on elevation mapping in Antarctica (Herzfeld et al., 1993, 2008, 1994; Herzfeld, 2004). Fig. 3 shows the DEMs derived from each of the retracked datasets over the Bering Glacier portion of the BBGS for Winter 2010/2011. For each dataset, we fit a unique Gaussian variogram model and extract the variogram parameters to optimally interpolate the dataset onto a $200m \times 200m$ grid, spanning all of Bering

Table 1
Valid elevation data points by region of the BBGS yielded by each level-2 processing method after the removal of outliers by the *raddev* filter.

Retracking method	Nov 2010–Apr 2011			May 2011–Oct 2011		
	Bering	Bagley	Total	Bering	Bagley	Total
ESA Baseline-C	588	115	703 (727)	750	319	1069
ESA Baseline-B	297	0	297 (303)	667	197	864
TFMRA Baseline-C	380	48	428 (451)	608	181	787
TFMRA Baseline-B	318	81	399 (430)	415	167	582
TFMRA Swath Baseline-C	72777	18513	93981 (112494)	117697	67386	185083
LMG Baseline-C	352	112	464 (477)	490	224	714

The amount of data points before the *raddev* filter was applied is given in parentheses for the November 2010 to April 2011 datasets. This time range reflects the approximate period of accumulation during the winter months (Trantow and Herzfeld, 2016). The datasets of aggregated measurements between May 2011 and October 2011 reflects the approximate period of ablation for the BBGS during the warmer months.

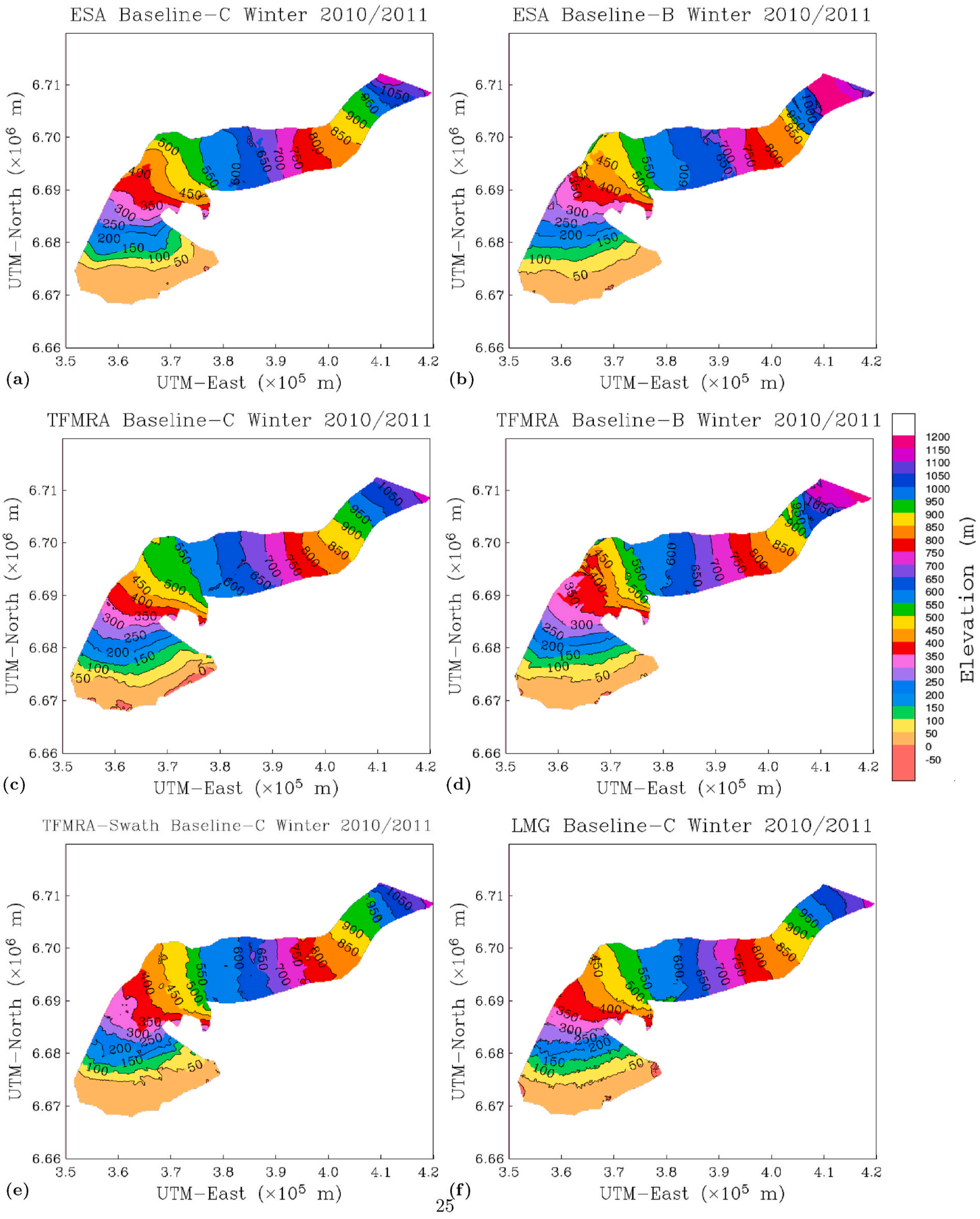

Fig. 3. Digital Elevation Model for each CryoSat-2 retracked dataset. (a) ESA Baseline-C, (b) ESA Baseline-B, (c) TFMRA Baseline-C, (d) TFMRA Baseline-B, (e) TFMRA Swath, and (f) LMG Baseline-C.

Glacier, using an advanced method of Ordinary Kriging which employs a quadrant search (Herzfeld et al., 2012). Each estimation uses input from a maximum of 16 nearby points, 4 points in each quadrant, within at most a 20 km radius. However, only 8 data points are used in the case of excellent local data coverage when there exists 2 data points in each surrounding quadrant within a 3 km radius around the estimation location.

Uncertainty in the kriging result at some point on the grid increases with the distance to the nearest measurement points used in estimation. This uncertainty reflects the data survey pattern, or spatial coverage, across the entire glacier and can be quantified by calculating the mean-distance-to-the-nearest-point for every location on the kriging grid. The uncertainty in the survey pattern can also be quantified by the Estimation Standard Deviation (ESD) error measure for kriging, as used in Trantow and Herzfeld (2016). However, the ESD measure also takes into account the fit of the Gaussian variogram model to the experimental variagram for a given data set. In the present analysis, we only quantify uncertainties arising from the particular characteristics of each retracked data set, and we therefore use the mean-distance-to-the-nearest-point measure rather than the ESD measure (see Section 4.1).

Each of the six CryoSat-2 DEMs is evaluated using the numerical random error measure, which quantifies the inherent noise in each dataset and its propagation through the Kriging equations (Herzfeld, 1992). Hereafter, we refer to this error measure as simply the *numerical error*. The numerical error measure is calculated for each elevation data point within a given retracked dataset following the equations in Trantow and Herzfeld (2016), which uses data noise estimates combined with the weights used in the kriging algorithm.

Noise estimates in the measurements are derived through a simple scaling of the *nugget* parameter (see Trantow and Herzfeld (2016), Section 6.2). The *nugget* is a geostatistical parameter derived from the experimental variogram, which deviates from zero as a consequences of noise in the measurements. The *nugget* is calculated for each data point by characterizing the deviation in height estimation with respect to nearby measurements in the same dataset, i.e., points within a 300 m radius. The 300 m size is equal to the CryoSat-2 SARIn along-track resolution and also equal to the lag-bin separation in the variogram analysis.

Note that the analysis in this paper does not investigate the effect that different interpolation schemes have on DEM generation. The kriging method has already been shown to be the ideal method for DEM derivation from CryoSat-2 data (Trantow and Herzfeld, 2016; Fei et al., 2017).

3.3. *Modeling of surge dynamics and crevassing*

A 3D finite element model of the Bering-Bagley Glacier System (BBGS) was created to simulate ice dynamics and glacial structure during the recent 2011–2013 surge (Trantow, 2014), and in particular for surge crevasses in Trantow and Herzfeld (2018), using the finite element software Elmer/Ice (Gagliardini et al., 2013). These previous studies have demonstrated the usefulness of Elmer/Ice in simulating and understanding surge mechanisms in the BBGS. In the current study, we focus on modeling the surge during the early-2011 phase, where results depend on the flow law, basal and lateral boundary conditions, a crevasse initiation criteria and input glacier geometry. The use of crevasses in model-data comparisons has allowed optimization of unknown model parameters important to simulate surging (Trantow and Herzfeld, 2018). Our goal here is to investigate the sensitivity of these optimized parameters to the different retracking methods.

The simulations presented in this paper are short diagnostic runs with a transient "relaxation" period, termed quasi-steady-state runs (Trantow and Herzfeld, 2018). For a full description of the BBGS model, along with justification for choices in model representations, see Trantow and Herzfeld (2018).

3.3.1. *Flow equations*

The model is governed by 3D Stokes flow,

$$\nabla \cdot \boldsymbol{\sigma} + \rho \boldsymbol{g} = \nabla \cdot (\boldsymbol{\tau} - p\boldsymbol{I}) + \rho \boldsymbol{g} = 0, \tag{1}$$

$$\nabla \cdot \boldsymbol{u} = tr(\dot{\varepsilon}) = 0, \tag{2}$$

where $\boldsymbol{\sigma}$ is the Cauchy stress tensor, $\boldsymbol{\tau}$ the deviatoric stress tensor, p the pressure, ρ the ice density, $\boldsymbol{g} = (0, 0, -9.81)$ the gravity vector, $\boldsymbol{u}$ the velocity vector and $\dot{\varepsilon} = \frac{1}{2}(\nabla \boldsymbol{u} + (\nabla \boldsymbol{u})^T)$ the strain-rate tensor. Equations (1) and (2) are linked via Glen's Flow Law assuming isothermal conditions as the BBGS is a temperate glacier system. A temperate glacier system implies that most of the BBGS ice is at the pressure melting point temperature throughout the year, which, for pressures experienced in the BBGS, leads to our prescription of an ice temperature of 0°C for experiments in this analysis (Trantow and Herzfeld, 2018).

3.3.2. *Boundary conditions*

The ice/atmosphere boundary at the upper surface is given as a stress-free boundary and is allowed to freely evolve. Forcing from both gravity and surface mass balance (SMB), that is, surface accumulation and ablation, cause the upper surface of the glacier to evolve. Surface height evolution is described by an advection equation, where changes in the upper surface elevation z_s are given by,

$$\frac{\partial z_s}{\partial t} + u_s \frac{\partial z_s}{\partial x} + v_s \frac{\partial z_s}{\partial y} - w_s = a_s, \tag{3}$$

where $\boldsymbol{u_s} = (u_s, v_s, w_s)$ is the surface velocity vector found from the Stokes equation (Equation (2)) and a_s is the accumulation or ablation component that is only prescribed in the direction normal to the surface (Gagliardini et al., 2013). Accumulation/ablation components are not included in the analysis of this paper due to the short timescales that are considered (100-day simulations maximally). That is, elevation changes are dominated by surge dynamics rather than accumulation or ablation during the major surge phase investigated in this analysis (Tangborn, 2013; Trantow and Herzfeld, 2016).

The most important aspect of modeling a surge relates to the treatment of the boundary condition at the base of the glacier via basal topography and the prescription of a sliding (or friction) law (Greve and Blatter, 2009; Cuffey and Paterson, 2010; Trantow and Herzfeld, 2018). For simulations of the early-2011 surge phase, we enforce a linear sliding law where normal velocities are set to zero and tangential velocities (u_t) are linearly proportional to shear stress (σ_{nt}) at the boundary:

$$\sigma_{nt} = \beta u_t. \tag{4}$$

The linear friction parameter β in Equation (4) is an unknown model parameter that can be estimated using crevasse-based model-data comparisons (Trantow and Herzfeld, 2018). A smaller β value corresponds to reduced friction at the glacier base, resulting from an increased amount of subglacial water Kamb (1987), which leads to basal sliding. Basal sliding accounts for most of the ice movement during a surge (Cuffey and Paterson, 2010; Trantow and Herzfeld, 2018). Optimized values for β are determined using crevasse-based model-data comparison methods, as discussed in Section 4.2.1.

The linear friction representation with uniform parameterization that we use in the current study is an appropriate approximation for the BBGS surge dynamics in a spatiotemporally-local sense, i.e., for a 100-day period of rapid acceleration in early 2011 across the model-data comparison domain ofof this analysis, as shown in Trantow and Herzfeld (2018) when comparing model results to observations. This assumption can be thought of as a steady-state assumption in the temporal sense and the consequences of this assumption on model results are investigated later in this paper (Section 4.2.1).

The lateral boundary condition also adopts a linear sliding law where the friction coefficient, β_{lat}, is set to fifty times the magnitude of basal friction coefficient, β, for each simulation in this analysis as this setting tends to best match observed stress patterns at the glacier margins as seen in the many model experiments of Trantow (2014) and in the results of Trantow and Herzfeld (2018). However, the lateral friction coefficient could be included as an additional model parameter to be optimized following the crevasse-based model-data comparison methods outlined in this paper.

3.3.3. *Crevasse initiation criterion and modeled crevasse characteristics*

The model estimates crevasse existence at a given nodal location by comparing the von Mises stress measure (σ_{vm}) at the ice surface to a given stress threshold ($\sigma_{threshold}$) (Trantow and Herzfeld, 2018),

$$\sigma_{vm} = \sigma_{1surf}^2 + \sigma_{2surf}^2 - \sigma_{1surf} \cdot \sigma_{2surf} > \sigma_{threshold}, \tag{5}$$

where $\sigma_{1surf} \geq \sigma_{2surf}$ are the two non-zero principal stresses in the surface plane (the third principal stress is normal to the surface plane and is assumed to be zero). Crevasse orientations are estimated to be normal to the modeled axis of maximum principal tensile stress within the surface plane. That is, a crevasse is assumed to open perpendicular to the principal stress axis corresponding to $\sigma_{1surf} > 0$. A $\sigma_{1surf} < 0$ corresponds to a compressional stress along the axis as opposed to an extensional or tensile stress. We assume extensional opening in our modeling of crevasses and the consequences of this assumption are discussed in Section 3.5. The stress threshold $\sigma_{threshold}$ in the von Mises criterion is another unknown model parameter that is estimated using the crevasse-based model-data comparisons (see Section 4.2.1).

3.3.4. *Input geometry*

Finally, the BBGS model depends on the input glacier geometry, which consists of basal and surface topographies. The basal topography input is given by a DEM (Trantow and Herzfeld, 2018) derived from ice-penetrating radar measurements made by the Jet Propulsion Laboratory's (JPL's) Warm Ice Sounding Explorer (WISE) in 2008 and 2012 over the BBGS (Rignot et al., 2013) (see Fig. 4). The derivation of the bed DEM follows the same kriging scheme as the surface DEMs, which is outlined in Section 3.2. The input surface topography is given by a DEM derived in Section 3.2 from one of the retracked CryoSat-2 SIRAL datasets (see also, Trantow and Herzfeld (2016)). The Elmer/Ice software interpolates the input DEMs, given at $200m \times 200m$ resolution, to the finite element grid, which for experiments in this analysis is at 400 m element-side-length resolution in the horizontal plane. An extruded mesh structure is employed with 5 vertical layers giving a vertical resolution varying between 2 and 300 m depending on location.

3.4. *Crevasse characteristics from image analysis*

Next, we derive crevasse location and orientation using image analysis allowing direct comparisons with modeled results. Using geostatistical methods applied to Landsat-7 panchromatic imagery (15 m resolution), we are able to determine crevassed areas and dominant orientations of the large surge-induced crevasses on a $600m\times 600m$ grid. The grid size was chosen to be somewhat larger than the model resolution so that modeled results could be averaged across several nearby nodes during the model-data comparison. Clouds tend to limit the amount of useable optical satellite imagery of the BBGS during the early-2011 phase. Moreover, striped artifacts exist in the Landsat-7 imagery due to instrument failure (Markham et al., 2004). However, we were able to find a Landsat-7 image from April 15, 2011 whose cloud- and stripe-free regions corresponded to the area of fresh surge crevasses (Fig. 5(a)). While Synthetic Aperture Radar (SAR) imagery may be better suited to resolve crevasse characteristics, as SAR images would be unaffected by cloud cover, we did not have access to any for the BBGS in 2011 at the time of the analysis. The intersection of this area with the model boundary provides the domain for the image analysis and the model-data comparisons (see the red line in Fig. 1 for the shape of this domain).

Crevasse locations are identified in imagery by applying a threshold to the geostatistical parameter mean-*pond*, which is derived from directional variograms calculated for 16 direction classes within a 400 m window centered on each grid point (or node) in the analysis domain (see Trantow and Herzfeld (2018) for more specifics on this calculation). The *pond* parameter is defined as the maximum of the experimental variogram (or vario-function, see Herzfeld (2008)), while the mean-*pond* parameter is the *pond* value averaged over all 16 directions. In general, all *pond* related parameters quantify ice-surface roughness. The natural logarithm of the mean-*pond* parameter is shown in Fig. 5(b) for the April 15, 2011 Landsat-7 image.

Crevasse orientations can also be identified in imagery using additional geostatistical parameters calculated from directional variograms (Trantow and Herzfeld, 2018). However, for the April 15, 2011 Landsat-7 image, crevasse orientations were assigned manually by classifying dominant crevasses at a particular nodal location into one of 16 evenly-spaced directional classes. Crevasse directional classes are labeled by the angle between the orientation vector and the east-west horizontal, implying an angle-range of $180^\circ/16 = 11.25^\circ$ for each class. Note that crevasse provinces, defined as areas homogeneous with respect to crevasse type and maximal with this property (Herzfeld et al., 2014), are typically much larger than $600m \times 600m$ for the BBGS (Herzfeld et al., 2013a). However, boundaries of crevasse provinces may exist within a $600m \times 600m$ analysis window which complicates crevasse orientation assignment. In this case we assign crevasse orientation to the dominant crevasses within the window. Orientation assignment was done at each of the crevassed locations determined by the *pond*-threshold (blue vectors in Fig. 5 (e)). The geostatistical image analysis approach is described in greater detail in Trantow and Herzfeld (2018).

3.5. *Crevasse-based model-data comparisons*

Crevasse characteristics derived in the image analysis given above can be directly compared to model results when using the model-data comparison methods derived in Trantow and Herzfeld (2018). Here,

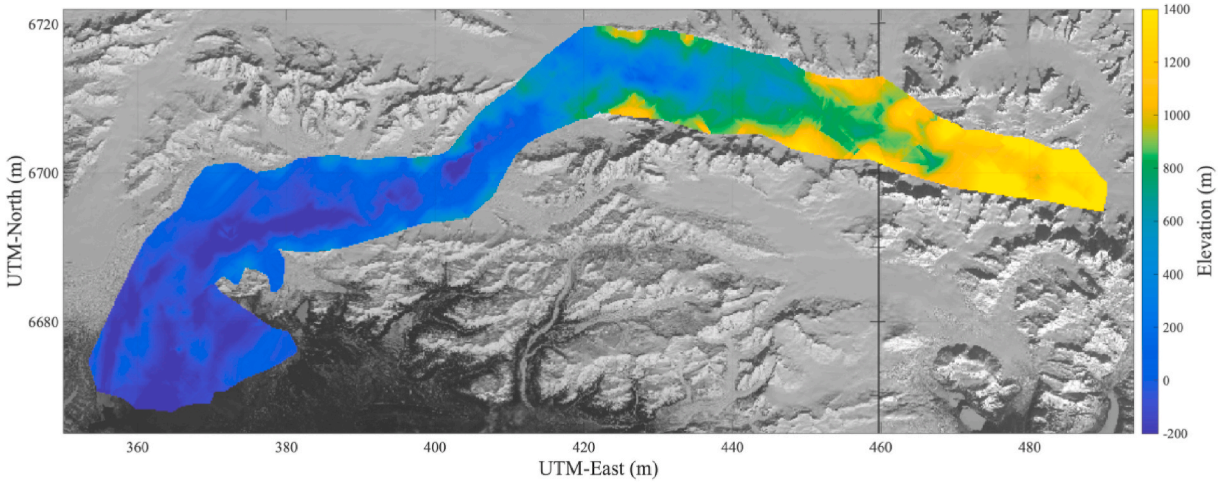

Fig. 4. Bed topography DEM for the BBGS model. Bed elevation was measured by JPL's WISE instrument and krigged to a $200m \times 200m$ DEM for use in the BBGS model simulations.

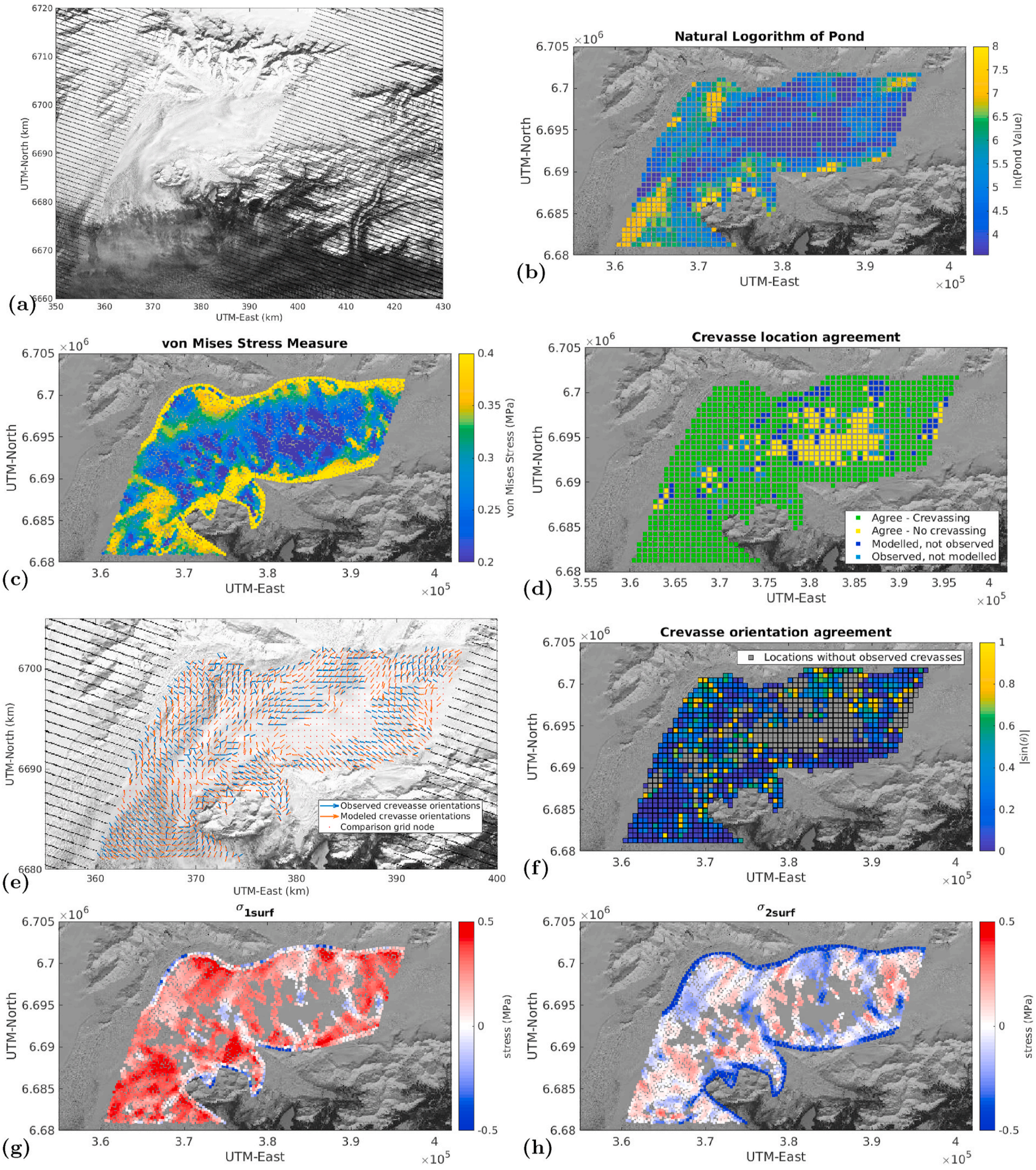

Fig. 5. Crevasse-based model-data comparisons using Landsat imagery and the BBGS model initialized with LMG-Baseline-C surface topography. (a) Landsat-7 panchromatic image form April 15, 2011 of Bering Glacier used to derive crevasse characteristics from observational sources during the surge in early 2011. (b) The natural logarithm on the mean-*pond* parameter derived from the Landsat image in (a). (c) The von Mises stress measure (σ_{vm} calculated from the model experiment initialized with LMG-Baseline-C topography after 50 1-day time steps. (d) Crevasse location comparison for the LMG model experiment at 50 days. (e) Crevasse orientations derived from the Landsat image in (a) (blue) and from the LMG model experiment (orange). (f) Crevasse orientation comparison for the LMG model experiment after 50 time steps. (g) The maximum principal surface stress for the LMG model experiment after 50 time steps. (h) The second principal surface stress for the LMG model experiment after 50 days. (For interpretation of the references to color in this figure legend, the reader is referred to the Web version of this article.)

we give an overview of these comparison methods using as an example the modeled crevasse location and orientation results from the model experiment that employs the input surface DEM derived from the LMG-Baseline-C dataset at day 50 of the simulation (see Fig. 5). Note that modeled results are mapped from their finite element grid to the image analysis grid within the analysis domain using an interpolation scheme based on a weighted-distance measure applied to neighboring points (Trantow and Herzfeld, 2018).

We use two comparison methods of crevasse location and crevasse orientation to optimally determine two important unknown model parameters: the basal friction coefficient (β in Equation (4)) and the von Mises stress threshold ($\sigma_{threshold}$ in Equation (5)). In the first comparison of crevasse location, disagreement is quantified by finding the fractional amount of nodes where model and observational data analysis disagree on crevasse existence. This quantity is given by the scalar α_1, defined as:

$$\alpha_1 = \frac{N_{disagree}}{N_{total}} \in [0,1] \tag{6}$$

where $N_{disagree}$ is the amount of nodes where model and observations disagree on crevasse existence and N_{total} is the total amount of nodes in the study domain. For the analysis in this paper and in Trantow and Herzfeld (2018), $N_{total} = 1185$ nodes.

This second scalar measure quantifying mean orientation discrepancy is given by α_2 and defined as:

$$\alpha_2 = \frac{\sum_{i=1}^{N_{crev}} |sin(\theta)|}{N_{crev}} \in [0,1] \tag{7}$$

where θ is the angle between unit orientation vectors derived from observations and the model, $\overrightarrow{v}^{obs}$ and $\overrightarrow{v}^{mod}$ respectively, and $N_{crev} = 898$ is the number of nodal locations where crevasses existence is consistent between the model and observations for this example.

A simple cost function C is used to combine α_1 and α_2, with associated weights w_1 and w_2 into a single scalar value to evaluate overall agreement:

$$C(\alpha_1, \alpha_2) = w_1 \cdot \alpha_1 + w_2 \cdot \alpha_2 \tag{8}$$

The cost value C is calculated for a number of model runs each with a unique set of parameter values for β and $\sigma_{threshold}$. Optimal parameter values are those associated with a minimized cost value and are denoted by an asterisk superscript (e.g., β^*). Fig. 5 (c) and (f) show the results of the comparison methods for the optimized parameter combination $\beta^* = 10^{-5}\frac{MPa \cdot a}{m}$ and $\sigma^*_{threshold} = 235$ kPa for a model simulation that uses the LMG-Baseline-C surface DEM as input after 50 1-day iterations.

For the analysis in this paper, we set the weights to be $w_1 = 4$ and $w_2 = 1$. The reason for weighing crevasse orientation comparisons lower than crevasse location comparisons ($w_2 < w_1$) does not stem from an undervaluation of matching orientations, but rather from experimentation in Trantow and Herzfeld (2018) where we found a small (negative) correlation between α_2^* and the magnitude of the optimized von Mises stress threshold, leading to a bias toward larger threshold values. This effect is explained by the following:

We observe that in locations where the maximum tensile stress at the surface is much larger than the von Mises threshold stress ($\sigma_{surf1} \gg \sigma_{threshold}$), modeled crevasse orientations tend to align better with observed crevasse orientations, given by lower $|sin(\theta)|$ values (see Fig. 5 (f)–(h)). This occurs when there is a dominant principal surface stress $\sigma_{surf1} \gg \sigma_{surf2}$, which will always be caused by extensional forcing $\sigma_{surf1} > 0$. When a dominant extensional force exists, crevasse orientations are expected to align better (more perpendicularly) to the axis of maximum principal stress. However, at locations where σ_{surf1} is closer in magnitude to the second principal surface stress, σ_{surf2}, crevasses open via mixed-mode fracturing, as opposed to extensional fracturing only (Mode I) (Van der Veen, 1998, 1999). In the case of mixed-mode fracturing, the significant shearing component causes crevasse orientations to no longer align perpendicularly with the maximum principal stress axis, which we assume when modeling crevasse orientations. Therefore, when we increase the von Mises stress threshold ($\sigma_{threshold}$), we decrease the amount of estimated crevasses that have a significant σ_{surf2} component, i.e., crevassing likely formed via mixed-mode fracturing, and we naturally attain better crevasse orientation matching (a smaller α_2 value). It is for this reason that we set the cost function weight associated with crevasse orientation, w_2, to be significantly lower than the crevasse-location weight. Development of a more accurate crevasse orientation estimate in the case of mixed-mode fracturing will increase confidence in modeling crevasse orientations and will allow an increase in w_2.

3.6. Method for model sensitivity study

New in this paper is the method for studying the sensitivity of modeled surge crevasses in the BBGS to input surface topography. We investigate this sensitivity by asking the following questions: All else equal, (1) Does input surface topography change the optimized values for the linear basal friction coefficient, β^*, and the von Mises stress threshold, $\sigma^*_{threshold}$, and the simulation time at which they are found? (2) Do modeled results from the various input surface topographies converge to one another with respect to the spatial pattern of modeled von Mises stress, crevasse orientation estimates and surface elevation as simulation time progresses? (3) Does a particular CryoSat-2 processing method lead to modeled results that best match observed crevasse characteristics or are modeled results dominated by constraints independent of the retracking method used?

To answer these questions, we run 6 sets of model experiments that differ only in their input surface topographies derived from the retracking methods introduced in Section 3.1. We apply the parameter optimization scheme introduced in Section 3.5 within each set of modeling experiments in order to answer question (1). Each experiment set consists of crevasse characteristic simulations that use a unique combination of the von Mises stress threshold, varying between 170 kPa and 250 kPa (Vaughan, 1993; Forster et al., 1999) at increments of 5 kPa, and a basal friction coefficient varying between $10^{-4.5}\frac{MPa \cdot a}{m}$ and $10^{-5.5}\frac{MPa \cdot a}{m}$ (Trantow, 2014) at increments of 0.25 in the exponent. The simulations are run for 100 one-day time steps during which the ice-surface can "relax", that is, the surface can freely evolve after the input geometry is prescribed, being forced only by gravity. We perform the optimization procedure once every 10 time steps across each 100 day simulation. As a result, each experiment set, defined by their input surface topography DEM, yields a unique β^* and $\sigma^*_{threshold}$, along with a minimized cost function value C^*, at every 10-day increment. The final fully-optimized parameter values for each experiment correspond to the lowest overall cost value C^* across all simulation time, which are labeled $\beta^\dagger$ and $\sigma^\dagger_{threshold}$, with an associated cost value $C^\dagger$, and similarity measures $\alpha_1^\dagger$ and $\alpha_2^\dagger$. Note that the parameter values optimized across the time domain are referred to as the "fully-optimized" parameter values. Since determination of the optimal von Mises stress threshold is done in post-processing, i.e., after the Elmer/Ice simulation has completed, we run only 5 model simulations per experiment corresponding to each of the tested basal friction coefficient values.

To investigate question (2), we compare results over the course of the full 100-day simulations that correspond to the fully-optimized basal friction coefficient, $\beta^\dagger$, for each experiment. At each 10-day time increment throughout the simulation, we compare the modeled von Mises stress, crevasse orientations (given by the maximum principal stress vector) and ice-surface elevation results from the six experiments to each other using the Map Comparison method covered in the following section. The value of $C^\dagger$, along with DEM uncertainty comparisons, will allow us to answer question (3).

3.7. Map Comparison Method

We investigate the convergence of the ice-surface estimates from the model experiments, with respect to one another, by employing the Map Comparison method (MAPCOMP) (Herzfeld and Merriam, 1990). The MAPCOMP method yields a similarity map given any finite number of input maps, which in our case are maps of model results from our six sets of experiments.

The MAPCOMP algorithm performs the similarity mapping by standardizing the input values of each input map and forming pairwise differences of the standardized values. To these differences, a semi-norm is applied, performed in a space whose dimension is equal to the number of possible pairwise comparisons among a set of input maps, to provide a normalized similarity value at each shared grid location. Similarity values, or MAPCOMP values, close to 0 indicate high similarity among input maps at a given location. While the largest possible similarity value is 1, this value rarely exceeds 0.5 (Herzfeld et al., 2007; Trantow and Herzfeld, 2018). Moreover, while MAPCOMP can be applied to any number of input maps of different variables, each comparison made in the present study uses maps of the same modeled output variable. Therefore, similarity values are expected to be relatively low across the resulting similarity maps, with values mostly under 0.1 (see Section 4.2.2). Input maps have the option to be weighted by their importance or confidence, however, we assign equal weights to each of the maps in the comparisons made in this paper. With equal weighting and consistent map grids among our inputs, the semi-norm used in our map comparisons is equivalent to the L1-norm. The mathematical formulation of the MAPCOMP method is given in full in Herzfeld and Merriam (1990).

The MAPCOMP method has the advantage over a simple correlation calculation in that it produces a map of spatial similarities rather than a single scalar value. While the MAPCOMP method is not designed to identify outliers among the input maps, it has an advantage over typical correlation analysis in that it does not require information reduction before analysis allowing investigation of spatial relationships. In the end, the resultant similarity map will allow a spatial analysis of similarities and differences between the results of our model experiments helping elucidate reasons for their existence.

4. Results and discussion

In the following, we summarize the resulting effects of CryoSat-2 retracking techniques on higher level data analysis. These effects are demonstrated through application of our approach to the early-2011 surge phase of the BBGS using CryoSat-2 retracked datasets for the time period spanning November 2010 to April 2011. In Section 4.1 we summarize error and uncertainty estimates within each retracked dataset and DEM product, and proceed to quantify the effects on elevation and elevation-change analysis when using CryoSat-2-derived DEMs via a series of difference maps between the various Bering Glacier DEMs. In Section 4.2, we analyze differences in numerical modeling results with respect to parameter estimation and in inter-model convergence of estimates of von Mises stress, crevasse orientations and surface elevation.

4.1. *Effects on DEM generation and elevation-change analysis*

4.1.1. *Error estimates*

Ice-surface DEMs are evaluated using the numerical error measure, which reflects the inherent noise within each dataset and its propagation through the kriging algorithm. The mean and standard deviation of the numerical error, along with noise and *nugget* values, are given in Table 2 for each DEM. In addition, we include the average distance from the estimation locations within the Bering Glacier DEM grid to the nearest data point used in kriging for each of the associated retracked datasets. The mean separation distance reflects the survey distribution across the entire glacier and may be interpreted as a measure of uncertainty in DEM generation. There is a clear negative correlation between the mean separation distance and the amount of data points within each POCA-based dataset, i.e., a higher number of data points yields a lower mean separation distance, as shown in Table 1.

The average numerical error is around 2 m for each dataset, which is much lower than the observed elevation changes occurring during the early-2011 phase of the BBGS surge, which exceed 60 m in several locations (Herzfeld et al., 2013b). As shown in Trantow and Herzfeld (2016), the dominant error in the CryoSat-2 DEMs stem from the survey pattern and therefore datasets with larger mean-distance measures, and a generally lower amount of data points, result in larger elevation uncertainty (e.g., the two Baseline-B datasets).

The LMG Baseline-C dataset provides the lowest average numerical error, which reflects more consistent elevation estimates between nearby points within the six-month dataset. Interestingly, the two Baseline-B datasets have the next lowest mean numerical error, which may be a reflection of the lower amount of data points. The Baseline-C processing chain provides more elevation estimates than the Baseline-B chain, independent of the retracking method used. Therefore, the set of additional estimates given by the Baseline-C processing are likely more noisy than the remaining data, leading to (mostly) higher associated numerical error and noise estimates.

Table 2
Error analysis means and standard deviations.

Season	Mean distance to nearest point (m)	Numerical error (m)	Noise (m)	Nugget (m^2)
ESA Baseline-C	878.38	1.94 ± 3.46	5.65 ± 11.24	78.99 ± 304.63
ESA Baseline-B	1886.96	1.25 ± 3.70	4.68 ± 13.00	95.09 ± 742.76
TFMRA Baseline-C	1285.24	2.04 ± 3.03	7.97 ± 11.28	95.16 ± 268.35
TFMRA Baseline-B	1329.30	0.86 ± 1.41	3.43 ± 5.90	23.22 ± 107.31
TFMRA Swath Baseline-C	535.32	2.04 ± 1.39	9.07 ± 6.17	60.03± 108.81
LMG Baseline-C	1037.65	0.82 ± 1.03	2.61 ± 3.30	8.83 ± 29.75

Noise estimates are found by scaling the *nugget* value calculated for each measurement within a data set. The numerical error is calculated using the noise estimates together with the kriging weights used in DEM generation (see Section 3.2 and Trantow and Herzfeld (2016)). The nearest distance measure reflects uncertainties in the DEMs arising from the survey error, i.e., the data distribution within each data set.

The swath processed dataset contains 100–250 times more elevation estimates compared to POCA datasets (Table 1), and as a result, provides a lower mean search distance for kriging by a factor of 2–4. However, the noise and numerical error estimates are largest in the TFMRA Swath dataset (along with the TFMRA Baseline-C dataset). The error analysis results are influenced by the ability of the *raddev* filter to remove phase-wrapped data points and therefore the relatively large noise estimates in the TFMRA Swath dataset stem from the large amount of phase-wrapped data that result during processing. However, without a reliable ambiguity DEM for Bering Glacier during surge, we must expect some amount of phase-wrapped data to exist in each dataset and the noise and numerical error estimates must still be taken into account when selecting a retracked dataset to use during higher level data analysis.

The numerical error is visualized in Fig. 6 for each Winter 2010/2011 dataset over Bering Glacier. Note that numerical error estimates can only be attained for data points that contain at least one other data point within a 300 m radius. Points that do not meet this requirement are given by an empty red marker in Fig. 6.

4.1.2. *Difference maps*

After quantifying the uncertainties in each DEM, we take a look at actual elevation differences between the Bering Glacier DEMs generated by the different retracking techniques (Figs. 7–9). Locations of the largest elevation discrepancy typically correspond to sparsely surveyed areas in one or both of the differenced DEMs. We identify large differences between Baseline-B DEMs and Baseline-C DEMs in upper Bering Glacier near the junction of Bagley Ice Field (Figs. 7(a),(c), 8(a),(b),(e), and 9(a),(c),(d)). This may be due to the location of Bering Glacier near the ocean, with upper-Bering and the Bagley Ice Field being further away, where there is a transition between CryoSat-2's ocean and in-land masks, which led to the 59.959 m offset in the ESA Baseline-C data over Bering Glacier (Mannan, 2017).

In general, the ESA Baseline-B data provide a map with the lowest overall ice-surface elevation (Figs. 7(b) and 8(a),(e) and 9(c),(e)), while the TFMRA Baseline-C data result in the map with the highest overall

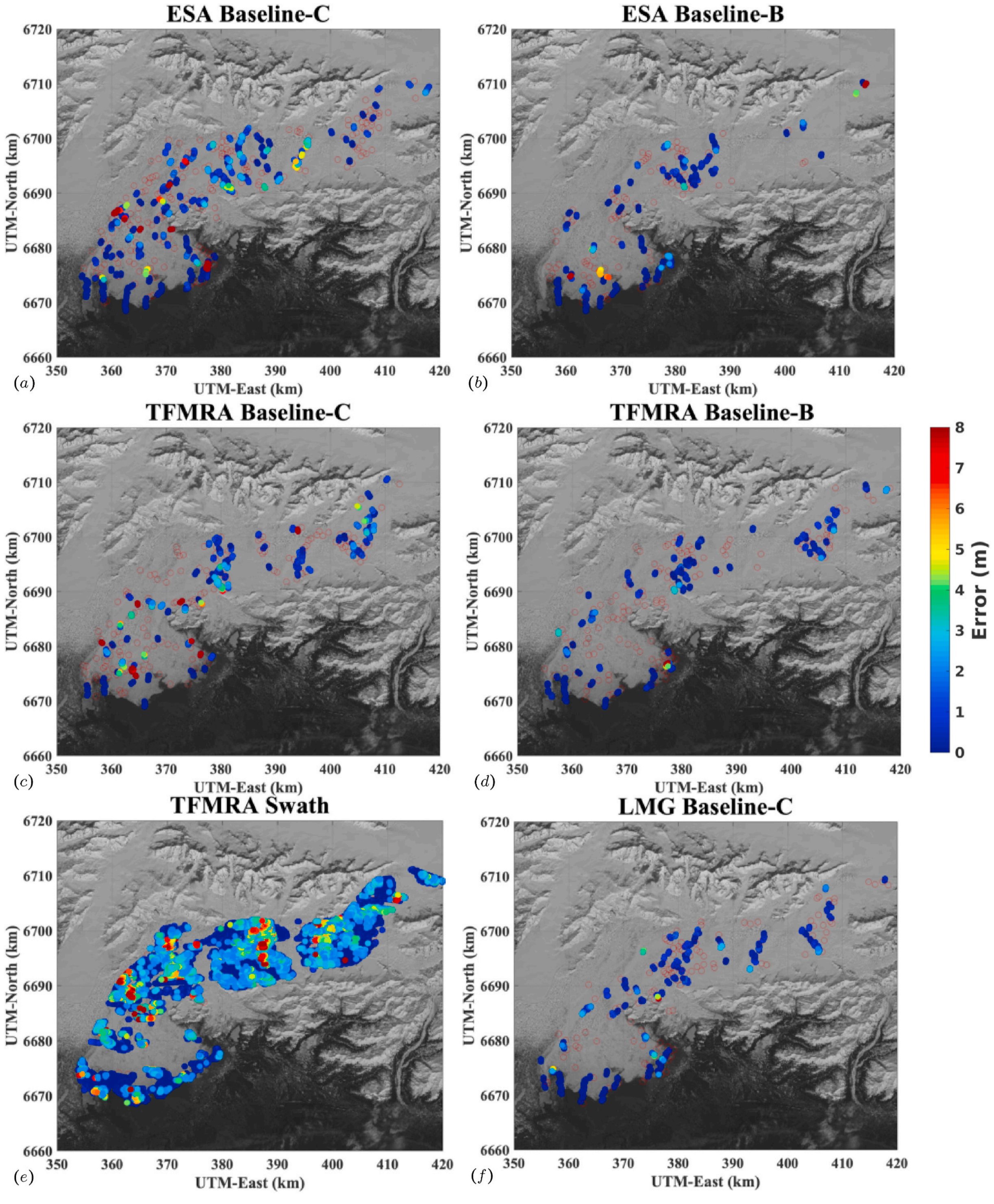

Fig. 6. **Numerical error from the propagation of the noise through the kriging algorithm**. Points marked by an empty red circle did not have any data points within a radius equal to the lag spacing and hence numerical error values are not calculated there. Numerical error estimates for the Winter 2010/2011 data are given for (*a*) ESA-Baseline-C, (*b*) ESA-Baseline-B, (*c*) TFMRA-Baseline-C, (*d*) TFMRA-Baseline-B, (*e*) TFMRA-Swath and (*f*) LMG-Baseline-C. Background image from LandSat-8 acquired on April 28, 2013. (For interpretation of the references to color in this figure legend, the reader is referred to the Web version of this article.)

elevation (Figs. 7(b) and 8(a)–(d)). The Khitrov Crevasse region (Fig. 1) is a location of consistent discrepancy between the various elevation maps, where some of the largest surge crevasses formed during the early-2011 phase of the surge (Herzfeld et al., 2013b; Trantow and Herzfeld, 2018). Many of the retracking methods are not able to supply elevation estimates in this region, which leads to larger interpolation discrepancies in the DEMs. Clearly, active crevassing occurring during the rapid surge acceleration complicates retracking, and consequently, elevation analysis, especially when aggregating data over a six-month period.

The figures show that large differences, upwards of 150 m, can exist between DEMs derived from different processing methods applied to CryoSat-2 measurements over heavily-crevassed and highly-sloped terrain and that one must be careful in their interpretation. However, as shown by the error-analysis in Trantow and Herzfeld (2016),

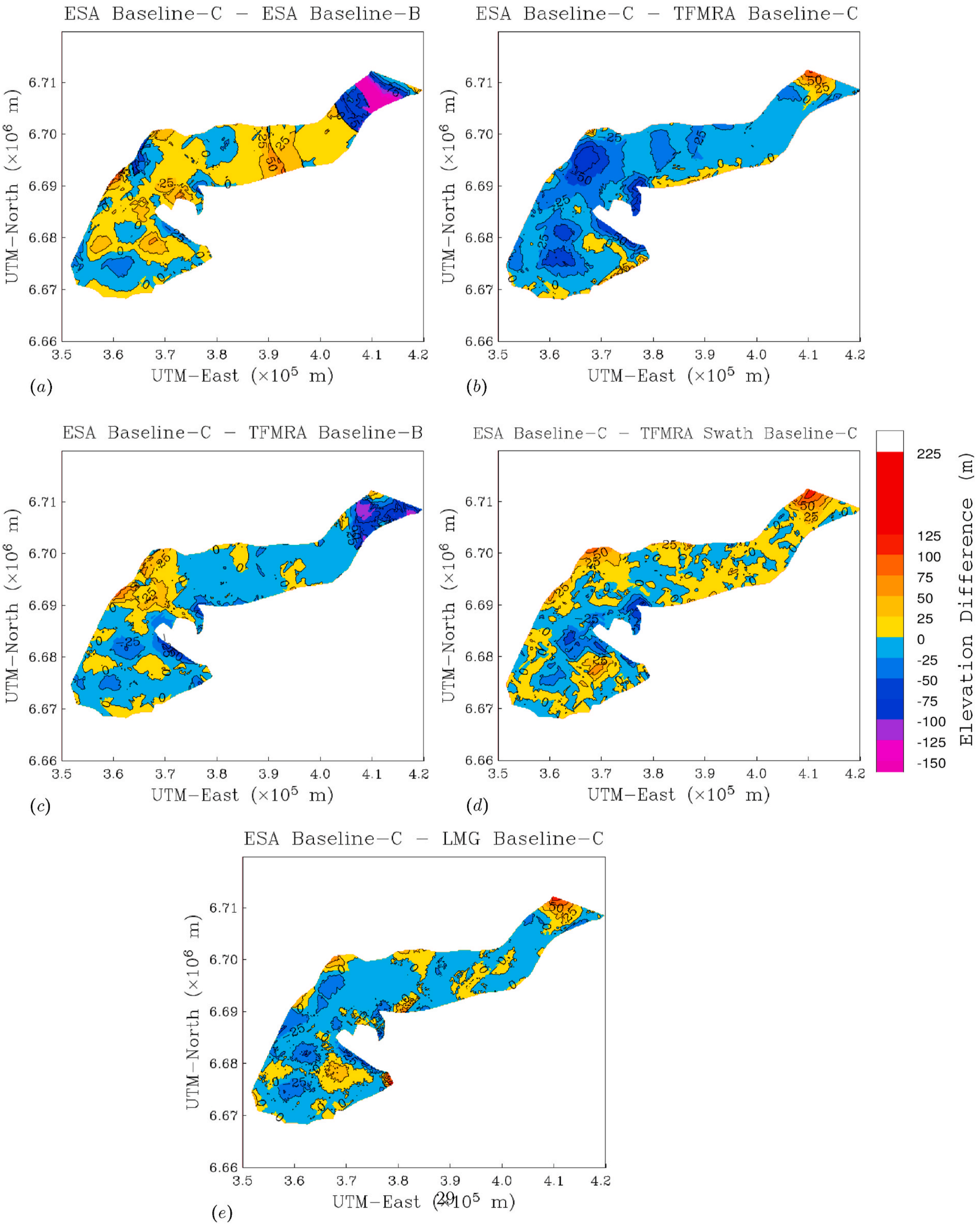

Fig. 7. Difference maps between various CryoSat-2 derived DEMs (part 1). (a) ESA-Baseline-C minus ESA-Baseline-B, (b) ESA-Baseline-C minus TFMRA-Baseline-C, (c) ESA-Baseline-C minus TFMRA-Baseline-B, (d) ESA-Baseline-C minus TFMRA-Swath, and (e) ESA-Baseline-C minus LMG-Baseline-C.

large-scale elevation changes (>15–20 m) that occur during a surge can still be analyzed using CryoSat-2-derived DEMs. This result was concluded from error measurements calculated for ESA Baseline-B data for the BBGS in Trantow and Herzfeld (2016), and the additional error estimates derived in Section 4.1.1 for each additional retracked dataset are consistent with this finding. On the other hand, using similar DEMs for elevation analysis during quiescence is not recommended, as six-month elevation-changes are typically less than the associated DEM error estimates. It is therefore better to aggregate CryoSat-2 data over a longer time period when analyzing the smaller elevation-changes during quiescence, which would greatly reduce the error associated with the survey pattern, i.e., the error associated with the mean distance to the nearest point during kriging. Finally, as we show in the following sections and in Trantow and Herzfeld (2018), the CryoSat-2 DEMs remain

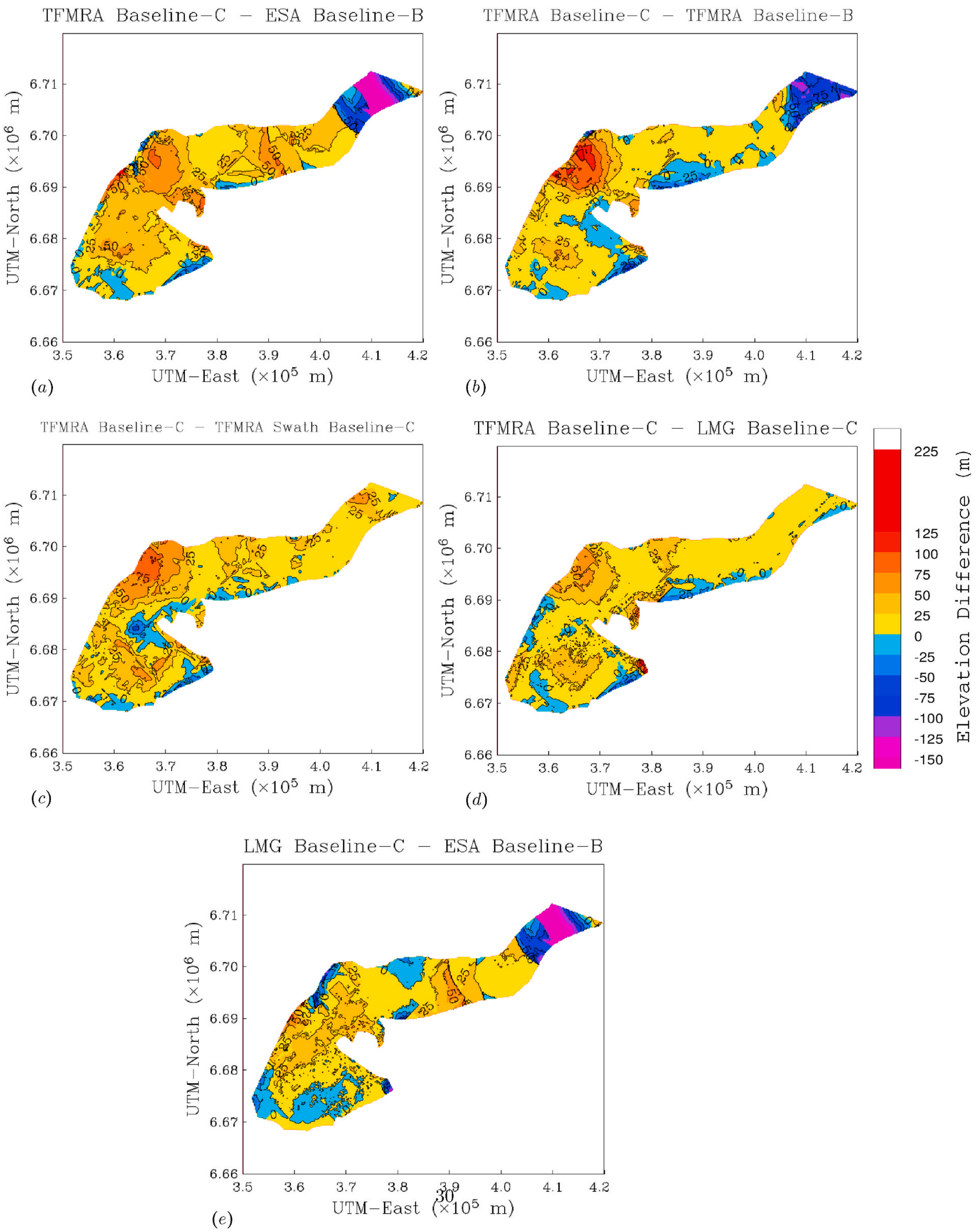

Fig. 8. Difference maps between various CryoSat-2 derived DEMs (part 2). (a) TFMRA-Baseline-C minus ESA Baseline-B, (b) TFMRA-Baseline-C minus TFMRA-Baseline-B, (c) TFMRA-Baseline-C minus TFMRA-Swath, (d) TFMRA Baseline-C minus LMG-Baseline-C, and (e) LMG-Baseline-C minus ESA-Baseline-B.

very useful as surface topography inputs for numerical models.

4.2. Effects on numerical modeling results

Next, we analyze the effects that a particular retracking technique has on numerical modeling results. Recall that each modeling experiment is given a unique CryoSat-2 surface DEM, corresponding to a particular retracking method, to initialize the ice-surface geometry.

4.2.1. Optimized model parameters

We begin by comparing parameter optimization results between the model experiments. Table 3 gives the fully-optimized values for the two important unknown parameters in the model, the von Mises stress threshold $\sigma^{\dagger}_{threshold}$ and the linear basal friction coefficient $\beta^{\dagger}$, and what

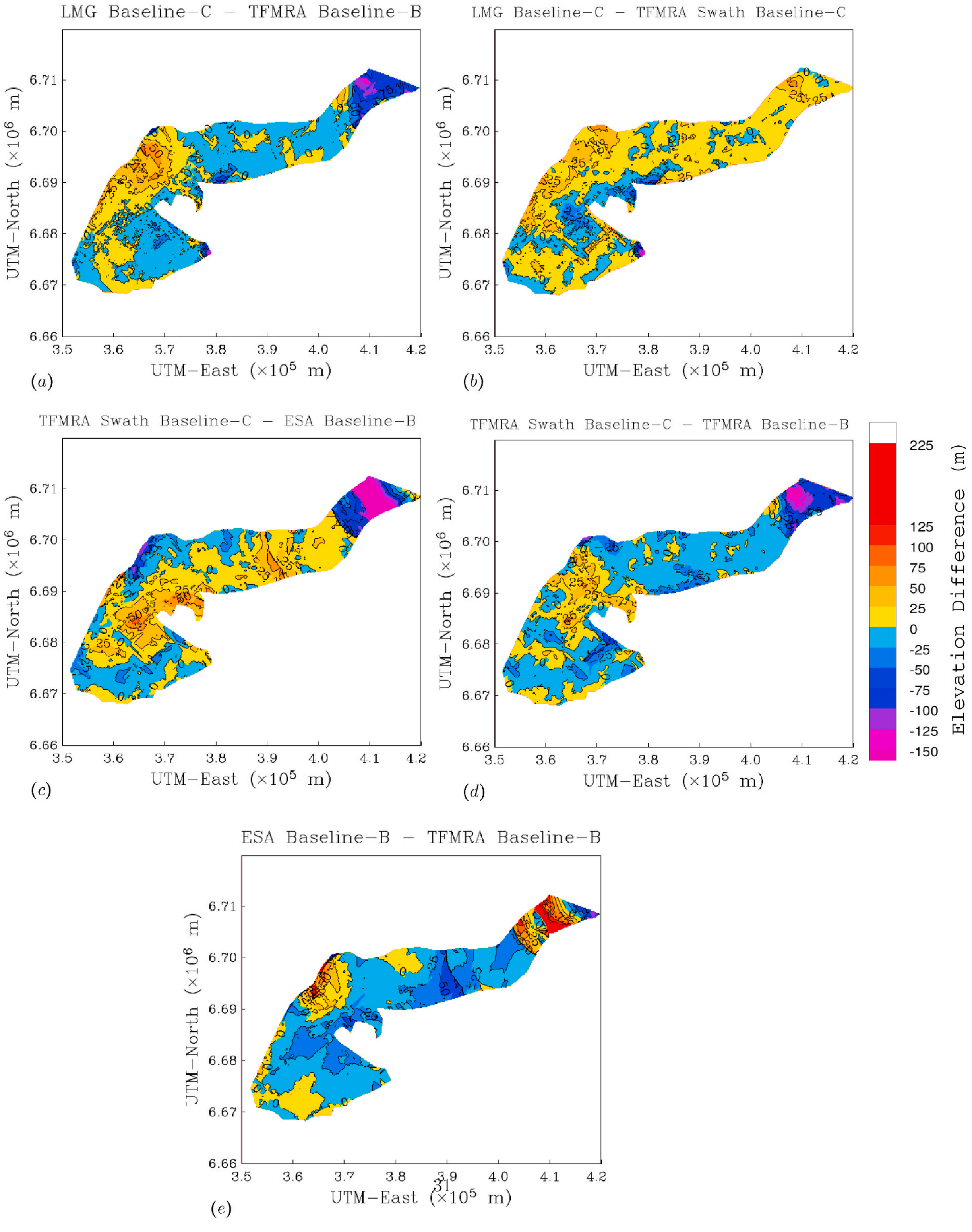

Fig. 9. Difference maps between various CryoSat-2 derived DEMs (part 3). (a) LMG-Baseline-C minus TFMRA-Baseline-B, (b) LMG-Baseline-C minus TFMRA-Swath, (c) TFMRA-Swath minus ESA-Baseline-B, (d) TFMRA-Swath minus TFMRA-Baseline-B, and (e) ESA-Baseline-B minus TFMRA-Baseline-B.

time in the simulation these optimized values are found. Recall that each simulation is run for 100 days using a 1-day time step size.

The general consistency of the optimal parameter estimates from each model experiment demonstrates that we are able to limit the effect of surface topography discrepancies from retracking differences when following the proper optimization routine, which is outlined throughout this section. Whichever CryoSat-2 surface DEM is given to the model, the fully-optimized basal friction coefficient is consistently $\beta^{\dagger} = 10^{-5}\frac{MPa\cdot a}{m}$. The consistency of the optimal basal sliding parameter across model experiments may allow increased precision in our estimate of $\beta^{\dagger}$ in future analysis by running additional model experiments that vary β values within a smaller range around $10^{-5}\frac{MPa\cdot a}{m}$. As shown in Trantow and Herzfeld (2018), a prescription of $\beta = 10^{-5}\frac{MPa\cdot a}{m}$ in the linear sliding

Table 3

Fully-optimized model parameter values given different input surface topographies. The parameter $\beta^\dagger$ is the fully-optimized basal sliding parameter in the linear friction law and $\sigma^\dagger_{threshold}$ is the fully-optimized von Mises stress threshold parameter in the von Mises criterion. The sixth column displays the mean von Mises stress, $\overline{\sigma}_{vm}$, across the analysis region for the model-data comparisons at the time corresponding to the lowest overall cost value. The final column gives the time step number (simulation day) for which modeled results and observations matched the best, as reflected by the lowest overall cost value, $C^\dagger$. The time step size is equal to 1-day.

Retracking method	$\beta^\dagger$ ($\frac{MPa \cdot a}{m}$)	$\sigma^\dagger_{threshold}$ (kPa)	$C^\dagger$	$\alpha_1^\dagger$	$\alpha_2^\dagger$	$\overline{\sigma}_{vm}$ (kPa)	Day of optimization
ESA Baseline-C	10^{-5}	235	1.0027	0.1181	0.5301	305.4	40
ESA Baseline-B	10^{-5}	235	1.0268	0.1266	0.5205	309.2	50
TFMRA Baseline-C	10^{-5}	240	1.0009	0.1173	0.5317	308.7	50
TFMRA Baseline-B	10^{-5}	235	1.0341	0.1257	0.5347	318.1	70
TFMRA Swath Baseline-C	10^{-5}	230	0.9956	0.1171	0.5280	300.3	20
LMG Baseline-C	10^{-5}	235	0.9947	0.1165	0.5288	308.6	50

law, together with ESA Baseline-C surface topography, results in modeled surface velocities that match the limited observations by an average of 0.54 ± 2.57 m/day, where average velocities were around 11 m/day. The velocity match provided an independent sanity check on the prescribed β value, and the results from the current analysis validate this parameterization further for simulation of the early-2011 surge phase within the model-data comparison domain.

In addition, the fully-optimized von Mises stress threshold, $\sigma^\dagger_{threshold}$, is remarkably consistent across the various model experiments with a few exceptions. The TFMRA retracking technique applied to the Baseline-C data, for both POCA and swath methods, were the only datasets that yielded an optimized von Mises stress threshold different than 235 kPa, at 230 kPa and 240 kPa respectively. However, both TFMRA Baseline-C experiments still yield relatively low cost measures, implying an excellent match to observations, and therefore we estimate the range of an optimal von Mises stress threshold to lie somewhere between 230 and 240 kPa. This estimated range of the von Mises stress threshold is slightly larger than the range of ice strength thresholds given by Forster et al. (1999) for temperate glaciers: 169–224 kPa. However, as discussed in Trantow and Herzfeld (2018), the stress threshold we derive here might better reflect the formation of crevasses of a particular size, which is associated with crevasse identification in the Landsat-7 imagery. Therefore, our optimized stress threshold could be larger than the stress threshold corresponding to brittle deformation that results in an initial fracture of the ice.

Note that the optimized stress threshold is assumed to be uniform through the analysis domain, but heterogeneous ice-characteristics may cause the ice yield strength to vary across the glacier surface. A non-uniform estimation carried out on a node-by-node basis (with some regularization) would lower the optimized cost function, and yield a better fit to observations, but at the risk of introducing more control parameters and degrees of freedom.

The LMG Baseline-C experiment, whose results yielded the lowest overall cost function, matched observed crevasse existence in 88.35% of locations within the model-data comparison domain. This excellent match lends further credence to the use of a linear friction law to represent surging in a spatiotemporally local sense. This result has motivated the development of a spatiotemporally evolving sliding law, based on a local linear representation, to simulate the entire progression of a BBGS surge (Trantow, 2020).

Table 3 shows that only the TFMRA Swath model experiment gives mean-von Mises stresses, $\overline{\sigma}_{vm}$, below 305 kPa across the analysis domain for model-data comparison. The lower overall surface stress given in this model experiment during the time of optimization is likely correlated with the lower estimate of the optimal von Mises threshold. This relationship is highlighted further in Fig. 10(a) and (b) which show that throughout each simulation the mean von Mises stress increases as do the estimates for the optimal threshold value. In other words, with larger overall surface stresses, a larger stress threshold is required in order to best match modeled and observed crevasses.

Next, we investigate the best time during the 100-day simulation for application of the optimization routine. In general, we find that the model best matches observations when optimal parameters are found after approximately 50 days of glacier evolution. Fig. 10 gives the estimate of the optimal von Mises stress threshold at various times throughout the 100-day simulation along with the associated model-data comparison measures α_1, α_2 and C. Fig. 10(a) reflects the increasing von Mises stress threshold with time-of-optimization that is associated with an increasing mean surface stress. The continued increase in mean surface stresses over time, as seen in Fig. 10(b), is a consequence of allowing our steady-state assumption to extend longer than is realistic during a surge. However, the cost value, after an initial decrease, also tends to increase with simulation time near the middle of the experiment (~50 days), depending on the exact model experiment, as seen in Fig. 10(e). This pattern reflects the evolution of the model-data crevasse location measure, α_1 (Fig. 10(c)), due to the relatively high weight given in the cost function. In general, the model-data crevasse orientation measure (α_2, Fig. 10(d)) decreases modestly after time zero for 20–40 iterations before remaining relatively constant across the simulation time (with the exception of the ESA Baseline-B experiment). As shown by the gray dashed line in subfigures (c)-(e), the difference measures α_1 and α_2, along with the overall cost value, are at a minimum at the 50 time-step mark when averaged over all model experiments. Moreover, the best time for optimization given by the model experiment with the lowest overall cost value, the LMG Baseline-C experiment, is shown to be at the 50-day mark (green line in Fig. 10(e)). These results suggest that the ideal time for performing the optimization procedure is around the 50-day time, i.e., after approximately 50 iterations, for the BBGS surge model when using a CryoSat-2 POCA input DEM. This time balances having enough simulation time elapse to elevate errors in the input surface DEM while still holding the steady-state assumption warranted for our investigation of the glacier state in early 2011.

The TFMRA Swath experiment gives optimal values after only 20 iterations, and therefore the additional elevation estimates given by swath processing may allow optimal parameter estimation after fewer model iterations. This also implies that actual elevation error in the swath-derived DEM may be lower than in the POCA-derived DEMs, with surface elevations more consistent with the other geometric representations given to the model (e.g., bed topography).

While Fig. 10(e) shows the range of possible cost values across time-of-optimization, Fig. 11 gives the range of cost values across the β-$\sigma_{threshold}$ parameter-space for the ESA Baseline-C experiment at 40 days. The overall lowest cost value, corresponding the fully-optimized parameter choice, is displayed in white text. The largest cost values, indicating the worst match to observations, are found where the linear friction coefficient is smallest ($10^{-5.5}\frac{MPa \cdot a}{m}$) and the von Mises stress threshold is largest (300 kPa), corresponding to simulations with the fastest glacier movement and strongest ice. Other parameter combinations that yield low cost values appear along the diagonal where ice yield strength is balanced with sliding speed. The fact that these cost

Fig. 10. Evolution of model and optimization values over each 100 day model simulation. ESA-Baseline-C (Red), ESA-Baseline-B (magenta), TFMRA-Baseline-C (black), TFMRA-Baseline-B (blue), TFMRA-Swath (cyan) and LMG-Baseline-C (green). The gray dashed line plots the mean value across all model experiments at each time. (a) The optimized von Mises stress threshold ($\sigma_{threshold}$). (b) Mean von Mises stress measure ($\overline{\sigma}_{vm}$) across the model-data analysis domain. (c) The model-data crevasse location difference measure (α_1). (d) The model-data crevasse orientation difference measure (α_2). (e) The minimized cost value associated with each time. (For interpretation of the references to color in this figure legend, the reader is referred to the Web version of this article.)

values along the diagonal are so close has motivated inclusion of additional data constraints to our optimization scheme, which includes the limited velocity data we have available during the surge in early-2011 (Trantow, 2020).

Note that the optimization of the model parameters in Trantow and Herzfeld (2018) were performed after 20 1-day iterations thus yielding an optimal estimation of $\sigma^*_{threshold} = 200kPa$. However, as seen in Fig. 10 (a), the estimation of the magnitude of $\sigma^*_{threshold}$ increases sharply when

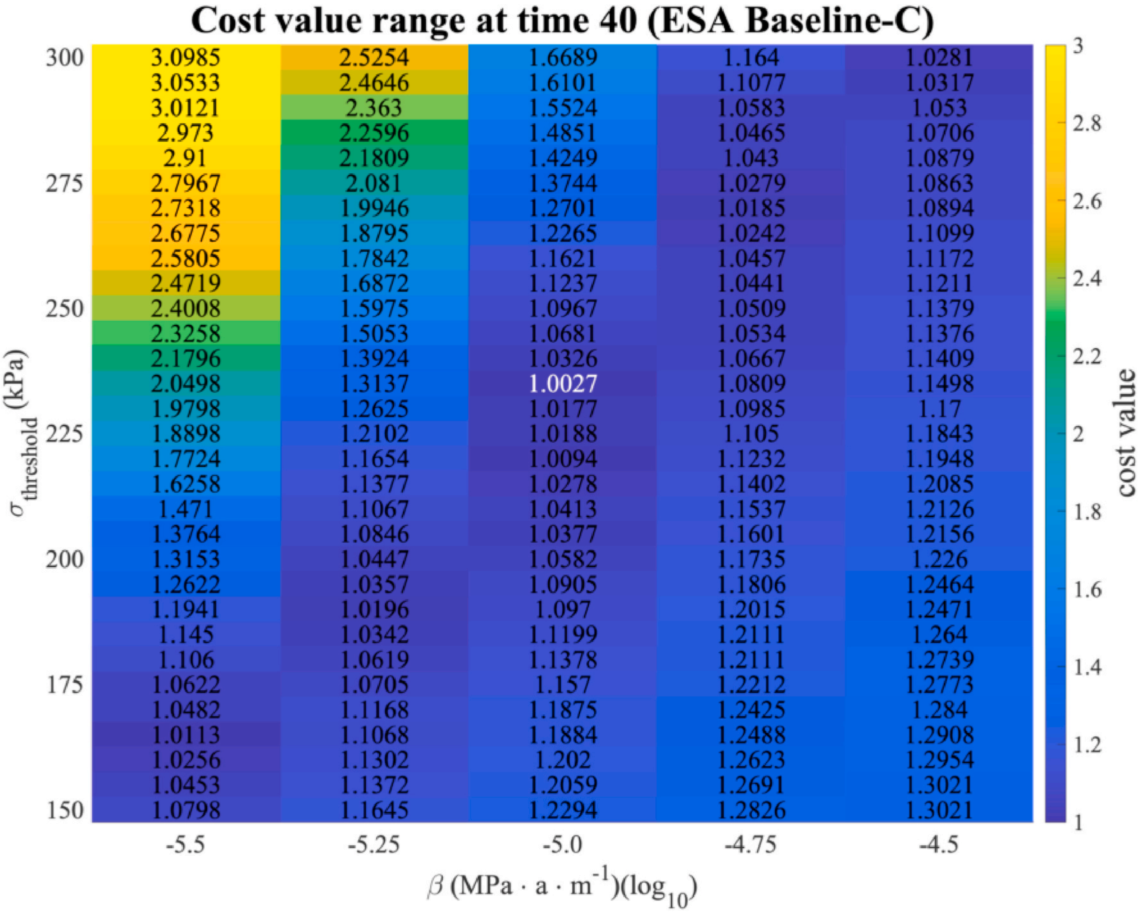

Cost value range at time 40 (ESA Baseline-C)

$\sigma_{threshold}$ (kPa)	-5.5	-5.25	-5.0	-4.75	-4.5
300	3.0985	2.5254	1.6689	1.164	1.0281
	3.0533	2.4646	1.6101	1.1077	1.0317
	3.0121	2.363	1.5524	1.0583	1.053
	2.973	2.2596	1.4851	1.0465	1.0706
	2.91	2.1809	1.4249	1.043	1.0879
275	2.7967	2.081	1.3744	1.0279	1.0863
	2.7318	1.9946	1.2701	1.0185	1.0894
	2.6775	1.8795	1.2265	1.0242	1.1099
	2.5805	1.7842	1.1621	1.0457	1.1172
	2.4719	1.6872	1.1237	1.0441	1.1211
250	2.4008	1.5975	1.0967	1.0509	1.1379
	2.3258	1.5053	1.0681	1.0534	1.1376
	2.1796	1.3924	1.0326	1.0667	1.1409
	2.0498	1.3137	1.0027	1.0809	1.1498
	1.9798	1.2625	1.0177	1.0985	1.17
225	1.8898	1.2102	1.0188	1.105	1.1843
	1.7724	1.1654	1.0094	1.1232	1.1948
	1.6258	1.1377	1.0278	1.1402	1.2085
	1.471	1.1067	1.0413	1.1537	1.2126
	1.3764	1.0846	1.0377	1.1601	1.2156
200	1.3153	1.0447	1.0582	1.1735	1.226
	1.2622	1.0357	1.0905	1.1806	1.2464
	1.1941	1.0196	1.097	1.2015	1.2471
	1.145	1.0342	1.1199	1.2111	1.264
	1.106	1.0619	1.1378	1.2111	1.2739
175	1.0622	1.0705	1.157	1.2212	1.2773
	1.0482	1.1168	1.1875	1.2425	1.284
	1.0113	1.1068	1.1884	1.2488	1.2908
	1.0256	1.1302	1.202	1.2623	1.2954
	1.0453	1.1372	1.2059	1.2691	1.3021
150	1.0798	1.1645	1.2294	1.2826	1.3021

Fig. 11. Range of cost values across the tested parameter-space for the ESA Baseline-C experiment at time = 40 days. The range of tested linear friction parameter values are given along the x-axis while the range of tested von Mises stress thresholds are along the y-axis. The magnitude of the cost value is specified by color and by the number within each cell. The cost value labeled in white text corresponds to the optimized value at day 40, which corresponds to the fully-optimized value across the space of possible β, $\sigma_{threshold}$, and time-of-optimization values. (For interpretation of the references to color in this figure legend, the reader is referred to the Web version of this article.)

performing the optimization 10–20 time steps later. The analysis in this section has shown that optimization closer to the 50-day mark yields better matches to observation, and therefore we favor the likely von Mises stress threshold for crevasse initiation to be closer to 235 kPa as found in this analysis, rather than 200 kPa as concluded in Trantow and Herzfeld (2018).

4.2.2. Convergence between model experiments

We are also interested in the effect that different retracking techniques have on longer transient simulations rather than only the diagnostic, parameter-optimization simulations we have run so far. In particular we ask, how long do noticeable effects caused by different input surface DEMs remain in the model as the simulation progresses in time when free surface evolution, forced only by gravity, is allowed as a characteristic of the model? This analysis looks at the convergence over the course of a 100 day simulation of three modeled variables at the glacier surface: (1) the von Mises stress, σ_{vm}, (2) the direction of the maximum principal stress axis, which determines modeled crevasse orientations, and (3) elevation. The map comparison (MAPCOMP) method is employed to quantify the spatial similarities of these parameters across the study region and determine how these similarities (or dissimilarities) change as the models run forward in time. Because comparisons (1) and (2) pertain to the modeling of crevasse characteristics, and ultimately their match to Landsat observations, the MAPCOMP analysis is performed only for modeled results within the model-data comparison domain. However, the third comparison of elevation also has relevance to the DEMs generated in Section 3.2 and therefore the associated MAPCOMP analysis is applied to modeled results for all of Bering Glacier.

4.2.2.1. von Mises stress. Fig. 12 shows the MAPCOMP results applied to the von Mises stress estimates given by the various model experiments, each using the basal friction coefficient $\beta = 10^{-5}$, after (a) a single 1-day time step, (b) after 30 days and (c) after 100 days. The mean MAPCOMP value across the entire study region is plotted against the number of model time steps in Fig. 12(d). While similarity values are below 0.1 throughout each map, indicating mostly high similarity between the von Mises maps from each model experiment, locations with relatively large similarity values still provide important spatial information with regards to model differences.

The results of these comparisons clearly indicate that the spatial pattern of von Mises stress converges between model experiments initialized with different surface topographies, with very little variance remaining after the simulations have run for 100 days. Fig. 12(a) shows that the model results after the first time step differ most significantly along the margins and at regions with large noise and numerical error estimates (see Fig. 6). Most notable is the Khitrov Crevasse region where the largest surge-crevasses were formed during the early-2011 phase of the surge. The region near 390 km UTM-East/6695 km UTM-North, where relatively large dissimilarity exist even after 30 days, corresponds to a region that is sparsely covered by height estimates for each of the retracked dataset, as seen in Fig. 2(a). This un-surveyed region

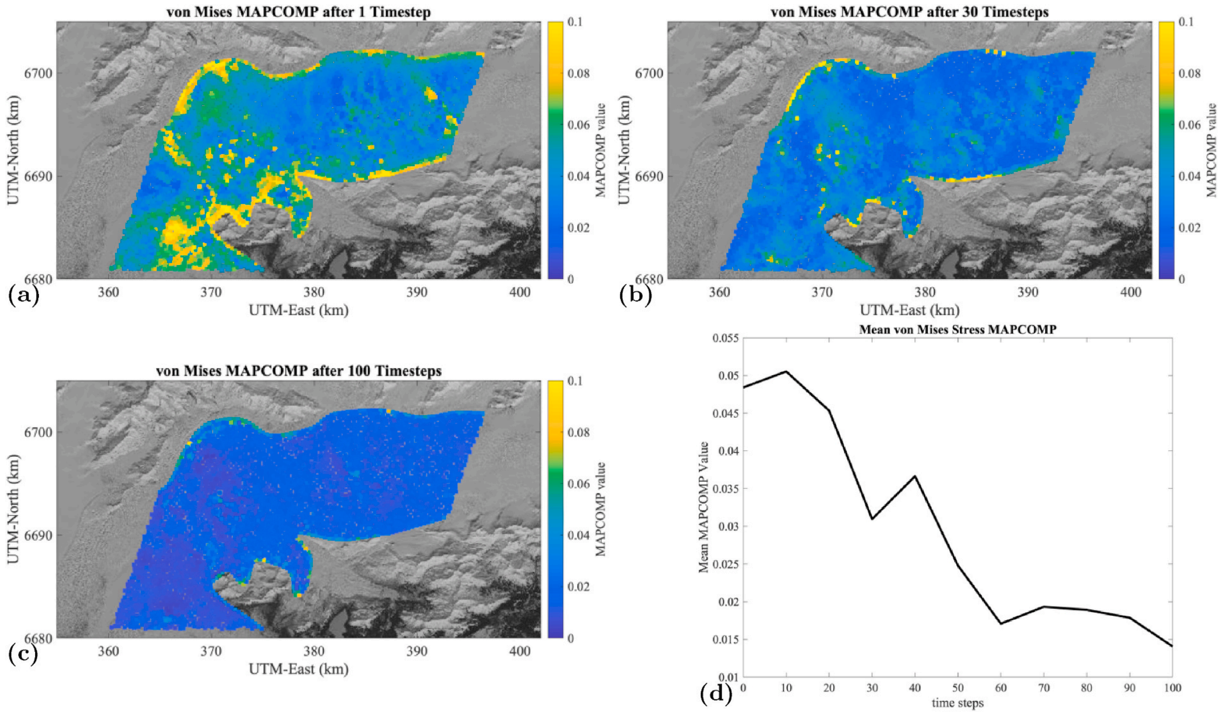

Fig. 12. MAPCOMP comparison of modeled von Mises stress at the ice surface between all six model experiments at different times during the simulation. (a) After a single 1-day time step. (b) After 30 1-day time steps. (c) After 100 1-day time steps. (d) Plot of the mean MAPCOMP value across all of Bering Glacier computed at 10-day increments throughout the 100-day simulation.

exists due to the CryoSat-2 satellite's flight pattern which does not fly over this location during the time period between November 2010 and April 2011. The large MAPCOMP values along the margins are mostly due to elevation estimation from kriging. Data points used in estimation can only be pulled from limited directions corresponding to the glacier mask. That is, we do not use elevations of the surrounding mountains and lakes in our estimation of glacier height.

In general, the results displayed in Fig. 12 indicate that spatial

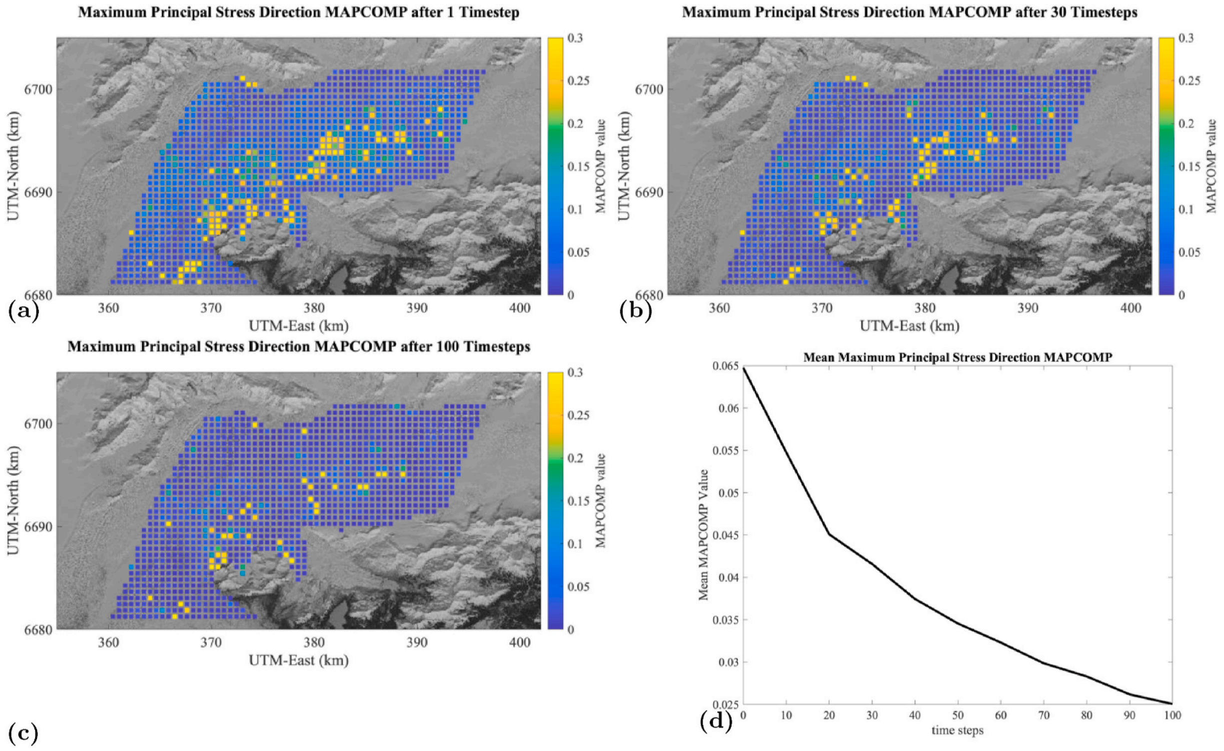

Fig. 13. MAPCOMP comparison of modeled maximum principal stress axis direction at the ice surface between all six model experiments at different times during the simulation. (a) After a single 1-day time step. (b) After 30 1-day time steps. (c) After 100 1-day time steps. (d) Plot of the mean MAPCOMP value across all of Bering Glacier computed at 10-day increments throughout the 100-day simulation.

variance of von Mises stress between model experiments is controlled largely by the satellite flight pattern and intrinsic interpolation restrictions. Discrepancies in modeled stress from different retracking techniques matters only in how the technique handles elevation estimation in the presence of large crevasses. Ultimately, the results from Section 4.2.1 indicate that optimization of the von Mises stress threshold is robust to these variances in the overall von Mises stress that arise from different retracking techniques as long as the recommended optimization procedure is followed.

4.2.2.2. Crevasse orientations and maximal principal stress axes. Fig. 13 displays the MAPCOMP result applied to the maximal principal stress axis directions from the six model experiments after (a) 1 day, (b) 30 days and (c) 100 days, while (d) shows the evolution of the mean MAPCOMP value across the entire domain over time. The appearance of larger MAPCOMP values, exceeding 0.3 in some locations, indicate less overall similarity of between modeled stress directions compared to modeled von Mises stress.

We find that the dissimilarities in the modeled maximal principal stress axis directions between model experiments reduce over the course of the 100-day simulation. The steady decrease in the mean-MAPCOMP measure reflects the increased dominance of other model aspects, likely basal topography, for determining the direction of maximal principal stress at the surface rather than initial surface topography. This is further shown by the widespread, near-zero MAPCOMP values (dark blue) that exist even after a single time step. However, while modeled crevasse orientations tend to converge in time across the six model experiments, they do not necessarily converge with respect to observations as shown in Fig. 10 (d). Model-data crevasse-orientation agreement would increase with improved bed-topography or, as mentioned previously, by incorporating mixed-mode fracturing in the modeled crevasse orientation determination.

It is interesting to note that the similarity of the modeled principal stress axes appear to converge at a similar rate to the von Mises stress. This result implies that differences, or errors, in the input surface topography are reduced at a similar rate with regards to their effect on stress orientations and stress magnitudes as the simulation time progresses. However, the mean MAPCOMP values corresponding to the stress directions are about 0.015 larger in magnitude than those associated with the von Mises stress, indicating a larger initial sensitivity to input surface topography. While this result may indicate larger uncertainties in modeling crevasse orientations compared to crevasse locations, which is reflected in our cost function weights α_1 and α_2, we emphasize that matches to orientation observations do not improve, and in fact mostly degrade, after 50 days, as reflected in the mean α_2 plot in Fig. 10 (d). Therefore, while the principal stress axes estimates continue to converge between model runs up to at least 100 days, we do not expect parameter optimization results to improve if the procedure is carried out after the 50-day mark.

The similarity maps show that relatively large dissimilarities in modeled crevasse orientations exist at isolated locations produced by the different input surface topographies, even after 100 days of surface evolution. The large region of dissimilarity at 382 km UTM-East/6693 km UTM-North is actually covered by a significant amount of height estimates for each retracked dataset (see Fig. 2). In this area in particular, we find that the POCA location (i.e., the x-y coordinate of the elevation estimate), identified in each retracking method, tends to avoid the large crevasses skirting the crevasse field boundary. This leads to a large discrepancy in the POCA location between the various retracking methods and also results in a significant information gap over the crevasse field. Therefore, this area could be used for investigation of CryoSat-2 data characteristics and retracking techniques in future analysis.

4.2.2.3. Elevation. Fig. 14 shows the evolution of the MAPCOMP measure applied to modeled surface elevation over Bering Glacier. Overall, the elevation similarity comparison yields by far the smallest similarity values indicating that the spatial patterns of modeled elevations

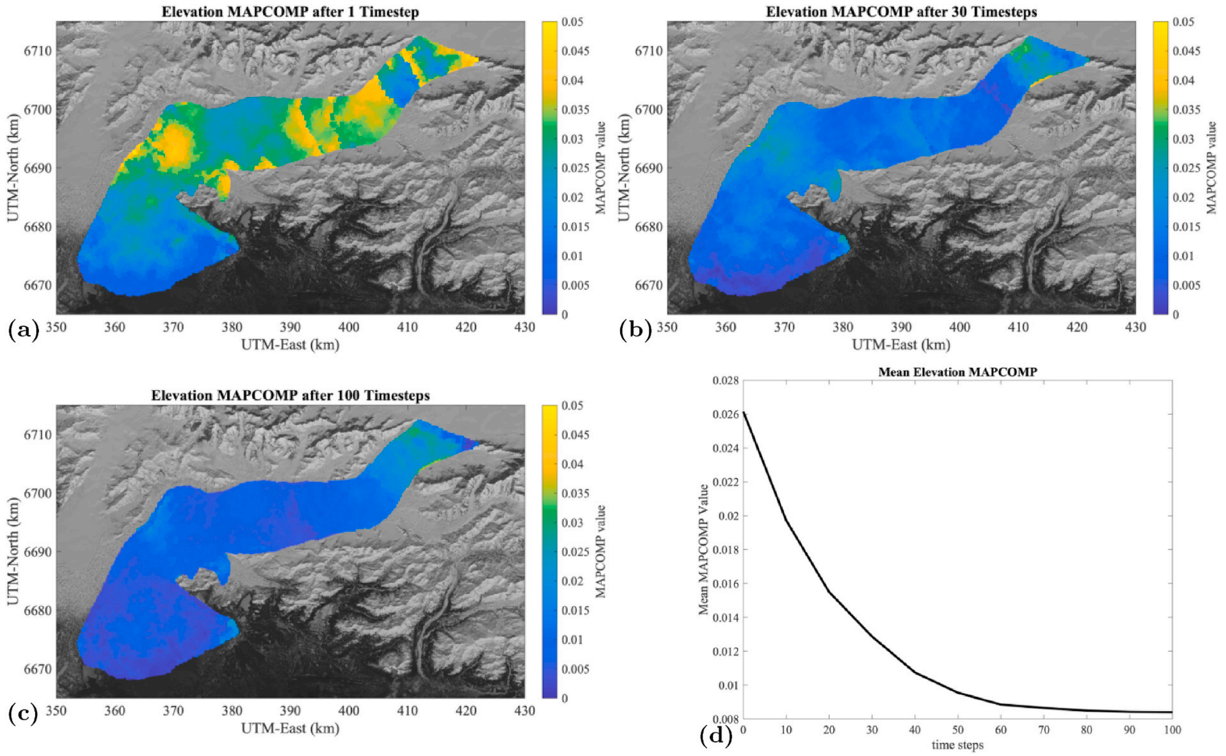

Fig. 14. MAPCOMP comparison of modeled surface elevation between all six model experiments at different times during the simulation. (a) After a single 1-day time step. (b) After 30 1-day time steps. (c) After 100 1-day time steps. (d) Plot of the mean MAPCOMP value across all of Bering Glacier computed at 10-day increments throughout the 100-day simulation.

estimates between experiments are more consistent compared to modeled stress magnitudes and directions. The most persistent modeled elevation differences manifest in upper Bering Glacier, where the Baseline-B DEMs differed most significantly to the Baseline-C DEMs (see Section 4.1.2).

We find that mean differences in the spatial pattern of modeled surface elevation decrease rapidly over the course of approximately 50 1-day time steps before leveling out. These results indicate that the spatial variances in modeled surface elevation caused by differences in initial surface topography tend to dissipate after a “relaxation” period of around 50 days during which the modeled ice surface can freely evolve. After this time period, the elevation pattern is less affected by peculiars in the input surface topography due to an increased influence of basal topography and other intrinsic aspects of the model (e.g., the glacial boundary, the isothermal assumption or the sliding law). The 50-day time period corresponds well to ideal time for performing the parameter optimization as determined in Section 4.2. We therefore recommend performing the parameter optimization routine after 50 days of free-surface evolution, regardless of the initial surface DEM used. This time period strikes a balance between reducing model effects from errors in the input surface DEM, computation time, and the ability of the DEM to realistically represent the glacier surface for the given time period (here Winter 2010/2011).

5. Summary and conclusions

Elevation estimations in the cryosphere have been greatly improved since the launch of ESA’s CryoSat-2 mission helping to reduce our uncertainties in estimating future global sea-level rise. Sea-level rise assessment is typically achieved through modeling, yet most ice-sheet-wide models are missing the implementation of different types of glacial acceleration, especially the most dramatic form, that of a surge. Here, we use numerical modeling in our assessment of CryoSat-2 data. In particular, we investigate the effects that differences in retracking techniques have on deriving and analyzing surface topography DEMs and numerical modeling results. We find the numerical error during DEM generation to range from 0.82±1.03 m for the LMG retracking method to 2.04±1.39 m for the TFMRA Swath method. The swath-processed dataset suffers from a large amount of phase-wrapping errors due to the lack of an unreliable ambiguity DEM for the BBGS during its surge phase in early 2011. However, the swath-processed dataset, by providing 100–250 times more data than the traditional POCA retracking methods, reduces the mean distance from the estimation location on the DEM grid to the nearest point by a factor of 2–4. With survey error dominating the uncertainties in DEM generation, we recommend using a swath-processed dataset, such as the TFMRA one used here, when analyzing elevation and elevation change in a large mountain glacier like the BBGS.

Difference maps between the various DEMs show that large differences upwards of 150 m can occur when using different retracked datasets for the heavily crevassed Bering Glacier. Therefore, large uncertainties in elevation and elevation-change analysis can exist, especially at sparsely surveyed locations, depending on which retracked dataset one chooses. We find that the largest differences between DEMs for Winter 2010/2011 exist between Baseline-B- and Baseline-C-based retracking methods, implying that lower level processing (level 0 or 1) account for a large portion of elevation estimation differences between the baseline processing chains. In general, crevasses complicate elevation derivation and can lead to significant information gaps over important crevassed regions that are critical to understanding the surge process.

In contrast to elevation-change analysis, we find that numerical modeling results related to parameter estimation can be relatively insensitive to differences in input surface topography DEMs arising from various retracking methods when following the proper optimization routine. The optimization of unknown model parameters is remarkably consistent across the six modeling experiments, with each yielding an optimal linear friction coefficient of $\beta^{\dagger} = 10^{-5}\frac{MPa \cdot a}{m}$ and an optimal von Mises stress threshold between $\sigma^{\dagger}_{threshold} = 230kPa$ and $240kPa$. The magnitude of our optimal stress threshold range is larger than that proposed for temperate glaciers by Forster et al. (1999) of 169–224 kPa. We find that the lowest overall cost measure, which quantifies the agreement between modeled and observed crevasse characteristics, to be associated with the LMG retracking method followed by the TFMRA Swath method. These results have helped to better parameterize our surge model during the most poorly constrained time period of the BBGS surge cycle corresponding to the major surge onset in early-2011. There is now less uncertainty in our model choices and parameterizations, which has led to further development of BBGS surge model (Trantow, 2020) and better understanding of the important surge mechanisms.

As a result of the MAPCOMP analysis, we find that the model experiments converge over time in their estimations of von Mises stress, crevasse orientations and elevation. These convergences suggests that differences in input surface DEMs arising from retracking methods have less of an effect on model results as simulation time proceeds. Model estimates of stress directions appear to be most sensitive to initial surface topography followed by stress magnitudes, while patterns of ice-surface elevation are least sensitive. The more persistant differences that remain between the model experiments after 100 days are attributed to the CryoSat-2 ground-track pattern during Winter 2010/2011, limitations in kriging ice elevations in mountainous regions and complications in retracking return-waveforms in highly crevassed regions. While differences between model experiments decrease over time, discrepancies between observations and model results generally show no improvement, or may in fact grow, after 40–60 days. We therefore recommend that the optimization procedure be performed after a relaxation period of 50 1-day iterations for POCA datasets. The improved spatial coverage provided by swath-processing may allow the parameter optimization routine to be carried out at an early time, e.g., after 20 days as given by the optimization results for the TFMRA Swath experiment.

All CryoSat-2 retracking methods are affected by crevassing and CryoSat-2 in general does not capture high-resolution surface roughness on the order of crevasses. Fresh surge crevasses in early-2011 led to relatively large noise and error estimates at particular locations within each dataset and between each dataset in terms of elevation estimates. However, the general consistency in modeling results after ~50 days of simulation may be explained by the fact that all retracking methods result in surface data of similar spatial characteristics.

Computer code availability

Code essential to the analysis in this paper is available on GitHub at the following public repository: https://github.com/trantow/bbgs_elmer. An example Solver Input File (SIF) to run the BBGS model in Elmer/Ice is provided (crev_BBGS_C2_swath_IAMG_20181126.sif) along with code the BBGS-specific User Functions (USF_Bering.f90). Code was written by Thomas Trantow and adapted from open source code provided by the Elmer/Ice community (see http://elmerice.elmerfem.org/courses-tutorials).

Data availability

Information on how to freely download the ESA-processed CryoSat-2 data is available online at https://earth.esa.int/web/guest/-/how-to-access-cryosat-data-6842. The TFMRA-processed CryoSat-2 data are available through V. Helm, while the LMG-processed data are available through J. Nilsson. The Landsat-7 data used in this analysis was downloaded using the USGS Global Visualization Viewer (GloVis) found at https://glovis.usgs.gov/.

Declaration of competing interest

Acknowledgements

We thank the International Association of Mathematical Geosciences for supporting this research through the Computers & Geosciences Student Scholarship Grant to the first author. Additional thanks are given to Steven Baker (University College London, UK), Mark Drinkwater, Tommaso Parrinello and Jerome Bouffard (all European Space Agency) for discussion of the 59 m offset in the CryoSat-2 Baseline-C data at the first CryoSat North American Science Meeting in Banff (Alberta, Canada). Thanks are also given to Eric Rignot (Jet Propulsion Laboratory, Pasadena, USA) and Jeremie Mouginot (University California Irvine, USA) for sharing their bed topographic data of the BBGS. Support of this research through the U.S. National Science Foundation's Arctic Natural Sciences Program (Award ARC-1148800), through U.S. National Science Foundation's Geography and Spatial Siences Program (Award GSS-1553133) and through NASA Cryospheric Sciences (Awards NNX17AG75G and NNX15AC73G) is gratefully acknowledged (U. Herzfeld is the PI of all awards).

References

Bamber, J., 1994. Ice sheet altimeter processing scheme. Int. J. Rem. Sens. 15, 925–938.

Bamber, J., Gomez-Dans, J.L., 2005. The accuracy of digital elevation models of the Antarctic continent. Earth Planet Sci. Lett. 237, 516–523.

Bamber, J.L., Huybrechts, P., 1996. Geometric boundary conditions for modelling the velocity field of the antarctic ice sheet. Ann. Glaciol. 23, 364–373.

Bentsen, M., Bethke, I., Debernard, J., Iversen, T., Kirkevag, A., Seland, O., Drange, H., Roelandt, C., Seierstad, I., Hoose, C., et al., 2012. The Norwegian earth system model, NorESM1-M-Part 1: description and basic evaluation. Geosci. Model Dev. Discuss. (GMDD) 5, 2843–2931.

Berger, M., Moreno, J., Johannessen, J.A., Levelt, P.F., Hanssen, R.F., 2012. ESA's Sentinel missions in support of earth system science. Remote Sens. Environ. 120, 84–90.

Bindschadler, R., Nowicki, S., Abe-ouchi, A., Aschwanden, A., Choi, H., Fastook, J., Granzow, G., Gutowski, G., Herzfeld, U., Jackson, C., Johnson, J., Khroulev, C., Levermann, A., Lipscomb, W.H., Martin, M.A., Morlighem, M., Parizek, B., Pollard, D., Price, S., Ren, D., Saito, F., Sato, T., Seddik, H., Seroussi, H., Takahashi, K., Walker, R., Wang, W.L., 2013. Ice-sheet model sensitivities to environmental forcing and their use in projecting future sea-level (the SeaRISE project). J. Glaciol. 59.

Bouffard, J., 2015. CRYOSAT-2: Level 2 Product Evolutions and Quality Improvements in Baseline C (V3).

Bouffard, J., Webb, E., Scagliola, M., Garcia-Mondéjar, A., Baker, S., Brockley, D., Gaudelli, J., Muir, A., Hall, A., Mannan, R., et al., 2017. Cryosat instrument performance and ice product quality status. Adv. Space Res. (3).

Brenner, A., Blndschadler, R., Thomas, R., Zwally, H., 1983. Slope-induced errors in radar altimetry over continental ice sheets. J. Geophys. Res.: Oceans 88, 1617–1623.

Brinkerhoff, D.J., Johnson, J., 2013. Data assimilation and prognostic whole ice sheet modelling with the variationally derived, higher order, open source, and fully parallel ice sheet model varglas. Cryosphere 7, 1161.

Burgess, E.W., Forster, R.R., Larsen, C.F., Braun, M., 2013. Surge dynamics on Bering Glacier, Alaska, in 2008–2011. Cryosphere 6, 1251–1262.

Clarke, G., 1987. Fast glacier flow: ice streams, surging, and tidewater glaciers. J. Geophys. Res. 92, 8835–8842.

Cuffey, K., Paterson, W.S.B., 2010. The Physics of Glaciers, fourth ed. Elsevier.

Davis, C.H., 1993. A surface and volume scattering retracking algorithm for ice sheet satellite altimetry. IEEE Trans. Geosci. Rem. Sens. 31, 811–818.

Davis, C.H., 1997. A robust threshold retracking algorithm for measuring ice-sheet surface elevation change from satellite radar altimeters. IEEE Trans. Geosci. Rem. Sens. 35, 974–979.

Dolgushin, L., Osipova, G., 1975. Glacier surges and the problem of their forecast. In: Symposium on snow and ice in mountain regions, vol. 104, pp. 292–304.

Esa, 2014. Cryosat Data Quality Status Summary, Tech. Rep. Cs-Tn- Esa-Gs-808 Version 7. European Space Agency.

Fatland, D.R., Lingle, C.S., 1998. Analysis of the 1993-95 Bering Glacier (Alaska) surge using differential SAR interferometry. J. Glaciol. 44, 532–546.

Fei, L., Feng, X., Sheng-Kai, Z., Dong-Chen, E., Xiao, C., Wei-Feng, H., Le-Xian, Y., Yao-Wen, Z., 2017. DEM development and precision analysis for Antarctic ice sheet using CryoSat-2 altimetry data. Chin. J. Geophys. 60, 231–243.

Foresta, L., Gourmelen, N., Pálsson, F., Nienow, P., Björnsson, H., Shepherd, A., 2016. Surface elevation change and mass balance of Icelandic ice caps derived from swath mode cryosat-2 altimetry. Geophys. Res. Lett. 43.

Forster, R.R., Rignot, E., Sacks, B.L., Jezek, K.C., 1999. Interferometric radar observations of glaciares europa and penguin, hielo patagonico sur, Chile. J. Glaciol. 45, 325–337.

Fowler, A., 1987. A theory of glacier surges. J. Geophys. Res. 92, 9111–9120.

Gagliardini, O., Zwinger, T., Gillet-Chaulet, F., Durand, G., Favier, L., Fleurian, B.d., Greve, R., Malinen, M., Martín, C., Raback, P., 2013. Capabilities and performance of Elmer/Ice, a new generation ice-sheet model. Geosci. Model Dev. Discuss. (GMDD) 6, 1689–1741.

Goelzer, H., Nowicki, S., Payne, A., Larour, E., Seroussi, H., Lipscomb, W.H., Gregory, J., Abe-Ouchi, A., Shepherd, A., Simon, E., et al., 2020. The future sea-level contribution of the Greenland ice sheet: a multi-model ensemble study of ISMIP6. Cryosphere Discuss. (1–43).

Goldberg, D.N., Sergienko, O.V., 2011. Data assimilation using a hybrid ice flow model. Cryosphere 5, 315–327.

Gourmelen, N., Escorihuela, M., Shepherd, A., Foresta, L., Muir, A., Garcia-Mondejar, A., Roca, M., Baker, S., Drinkwater, M., 2018. Cryosat-2 swath interferometric altimetry for mapping ice elevation and elevation change. Adv. Space Res. 62, 1226–1242.

Gray, L., Burgess, D., Copland, L., Cullen, R., Galin, N., Hawley, R., Helm, V., 2013. Interferometric swath processing of Cryosat data for glacial ice topography. Cryosphere 7, 1857–1867.

Gray, L., Burgess, D., Copland, L., Demuth, M., Dunse, T., Langley, K., Schuler, T., 2015. CryoSat-2 delivers monthly and inter-annual surface elevation change for Arctic ice caps. Cryosphere 9, 1895–1913.

Gray, L., Burgess, D., Copland, L., Dunse, T., Langley, K., Moholdt, G., 2017. A revised calibration of the interferometric mode of the Cryosat-2 radar altimeter improves ice height and height change measurements in western Greenland. Cryosphere 11, 1041–1058.

Greve, R., Blatter, H., 2009. Dynamics of Ice Sheets and Glaciers. Springer, Berlin, Germany etc.

Greve, R., Saito, F., Abe-Ouchi, A., 2011. Initial results of the searise numerical experiments with the models sicopolis and icies for the Greenland ice sheet. Ann. Glaciol. 52, 23–30.

Helm, V., Humbert, A., Miller, H., 2014. Elevation and elevation change of Greenland and Antarctica derived from cryosat-2. Cryosphere 8, 1539–1559.

Herzfeld, U., 1992. Least-squares collocation, geophysical inverse theory and geostatistics: a bird's eye view. Geophys. J. Int. 111, 237–249.

Herzfeld, U., 1998. *The 1993-1995 Surge of Bering Glacier (Alaska) — a Photographic Documentation of Crevasse Patterns and Environmental Changes* Volume 17 of *Trierer Geograph. Studien*. Geograph. Gesellschaft Trier and Fachbereich VI – Geographie/ Geowissenschaften. Universität Trier.

Herzfeld, U., Hunke, E., McDonald, B., Wallin, B., 2015. Sea Ice Deformation in Fram Strait — comparison of CICE simulations with analysis and classification of airborne remote-sensing data. Cold Reg. Sci. Technol. 117.

Herzfeld, U., Lingle, C., Lee, L., 1993. Geostatistical evaluation of satellite radar altimetry for high resolution mapping of Antarctic ice streams. Ann. Glaciol. 17, 77–85.

Herzfeld, U., McDonald, B., Wallin, B., Krabill, W., Manizade, S., Sonntag, J., Mayer, H., Yearsley, W., Chen, P., Weltman, A., 2014. Elevation changes and dynamic provinces of Jakobshavn Isbræ, Greenland, derived using generalized spatial surface roughness from ICESat GLAS and ATM data. J. Glaciol. 60, 834–848.

Herzfeld, U., McDonald, B., Weltman, A., 2013a. Bering Glacier and Bagley Ice Valley surge 2011: crevasse classification as an approach to map deformation stages and surge progression. Ann. Glaciol. 54 (63), 279–286.

Herzfeld, U., Wallin, B., Stachura, M., 2012. Applications of geostatistics in optimal design of satellite altimetry orbits and measurement configurations. J. Astronaut. Sci. 58, 495–511.

Herzfeld, U.C., 2004. Atlas of Antarctica: Topographic Maps from Geostatistical Analysis of Satellite Radar Altimeter Data, vol. 1. Springer Verlag.

Herzfeld, U.C., 2008. Master of the obscure — automated geostatistical classification in presence of complex geophysical processes. Math. Geosci. 40, 587–618.

Herzfeld, U.C., Lingle, C.S., Lee, L., 1994. Recent advance of the grounding line of Lambert Glacier, Antarctica, deduced from satellite-radar altimetry. Ann. Glaciol. 20, 43–47.

Herzfeld, U.C., Drobot, S., Wu, W., Fowler, C., Maslanik, J., 2007. Spatio-temporal climate model validation - case studies for MM5 over northwestern Canada and Alaska. Earth Interact. 11, 1–23.

Herzfeld, U.C., McBride, P.J., Zwally, H., Dimarzio, J., 2008. Elevation changes in Pine Island Glacier, Walgreen Coast, Antarctica, based on GLAS (2003) and ERS-1 (1995) altimeter data analyses and glaciological implications. Int. J. Rem. Sens. 29, 5533–5553.

Herzfeld, U.C., McDonald, B., Stachura, M., Hale, R.G., Chen, P., Trantow, T., 2013b. Bering Glacier surge 2011: analysis of laser altimeter data. Ann. Glaciol. 54 (63), 158–170.

Herzfeld, U.C., Merriam, D.F., 1990. A map comparison technique utilizing weighted input parameters. Comput. Geol. 7, 43–52.

Jiskoot, H., Pedersen, A.K., Murray, T., 2001. Multi-model photogrammetric analysis of the 1990s surge of Sortebrae, East Greenland. J. Glaciol. 47, 677–687.

Jungclaus, J., Fischer, N., Haak, H., Lohmann, K., Marotzke, J., Matei, D., Mikolajewicz, U., Notz, D., Storch, J., 2013. Characteristics of the ocean simulations in the Max Planck Institute Ocean Model (MPIOM) the ocean component of the MPI-Earth system model. J. Adv. Model. Earth Syst. 5, 422–446.

Kamb, W.B., 1987. Glacier surge mechanism based on linked cavity configuration of the basal water conduit system. J. Geophys. Res. B 92, 9083–9100.

Kay, J., Deser, C., Phillips, A., Mai, A., Hannay, C., Strand, G., Arblaster, J., Bates, S., Danabasoglu, G., Edwards, J., et al., 2015. The Community Earth System Model (CESM) large ensemble project: a community resource for studying climate change in the presence of internal climate variability. Bull. Am. Meteorol. Soc. 96, 1333–1349.

Larour, E., Utke, J., Csatho, B., Schenk, A., Seroussi, H., Morlighem, M., Rignot, E., Schlegel, N., Khazendar, A., 2014. Inferred basal friction and surface mass balance of North-East Greenland Ice Stream using data assimilation of ICESat-1 surface altimetry and ISSM. Cryosphere Discuss. 8, 2331–2373.

Larour, E.H., Seroussi, H., Morlighem, M., Rignot, E., 2012. Continental scale, high order, high spatial resolution, ice sheet modeling using the Ice Sheet System Model (ISSM). J. Geophys. Res. 117 (F1), F01022.

Lipscomb, W.H., Price, S.F., Hoffman, M.J., Leguy, G.R., Bennett, A.R., Bradley, S.L., Evans, K.J., Fyke, J.G., Kennedy, J.H., Perego, M., et al., 2019. Description and evaluation of the community ice sheet model (cism) v2. 1. Geosci. Model Dev. (GMD) 12, 387–424.

Mannan, R., 2017. CRYOSAT Ice Data Quality Status Summary.

Markham, B.L., Storey, J.C., Williams, D.L., Irons, J.R., 2004. Landsat sensor performance: history and current status. IEEE Trans. Geosci. Rem. Sens. 42, 2691–2694.

Markus, T., Neumann, T., Martino, A., Abdalati, W., Brunt, K., Csatho, B., Farrell, S., Fricker, H., Gardner, A., Harding, D., et al., 2017. The Ice, Cloud, and land Elevation Satellite-2 (ICESat-2): science requirements, concept, and implementation. Rem. Sens. Environ. 190, 260–273.

Marsiat, I., Bamber, J., 1997. The climate of Antarctica in the UGAMP GCM: sensitivity to topography. Ann. Glaciol. 25, 79–84.

Meier, M., Post, A., 1969. What are glacier surges? Can. J. Earth Sci. 6, 807–817.

Murray, T., Strozzi, T., Luckman, A., Jiskoot, H., Christakos, P., 2003. Is there a single surge mechanism? Contrasts in dynamics between glacier surges in Svalbard and other regions. J. Geophys. Res. 108, 2237.

Neumann, T.A., Martino, A.J., Markus, T., Bae, S., Bock, M.R., Brenner, A.C., Brunt, K.M., Cavanaugh, J., Fernandes, S.T., Hancock, D.W., et al., 2019. The ice, cloud, and land elevation satellite–2 mission: a global geolocated photon product derived from the advanced topographic laser altimeter system. Remote Sens. Environ. 233, 111325.

Nilsson, J., Gardner, A., Sandberg Sørensen, L., Forsberg, R., 2016. Improved retrieval of land ice topography from Cryosat-2 data and its impact for volume-change estimation of the Greenland ice sheet. Cryosphere 10, 2953–2969.

Nowicki, S., Bindschadler, R., Abe-ouchi, A., Aschwanden, A., Choi, H., Fastook, J., Granzow, G., Gutowski, G., Herzfeld, U., Jackson, C., Johnson, J., Khroulev, C., Levermann, A., Lipscomb, W.H., Martin, M.A., Morlighem, M., Parizek, B., Pollard, D., Price, S., Ren, D., Saito, F., Sato, T., Seddik, H., Seroussi, H., Takahashi, K., Walker, R., Wang, W.L., 2013a. Spatial sensitivities of the Greenland ice sheet to environmental changes (the SeaRISE project). J. Geophys. Res. Earth Surf. 1025–1044.

Nowicki, S., Bindschadler, R., Abe-ouchi, A., Aschwanden, A., Choi, H., Fastook, J., Granzow, G., Gutowski, G., Herzfeld, U., Jackson, C., Johnson, J., Khroulev, C., Levermann, A., Lipscomb, W.H., Martin, M.A., Morlighem, M., Parizek, B., Pollard, D., Price, S., Ren, D., Saito, F., Sato, T., Seddik, H., Seroussi, H., Takahashi, K., Walker, R., Wang, W.L., 2013. Spatial sensitivities of the Antarctic ice sheet to environmental changes (the SeaRISE project). J. Geophys. Res. Earth Surf. 1002–1024.

Nowicki, S.M.J., Payne, T., Larour, E., Seroussi, H., Goelzer, H., Lipscomb, W., Gregory, J., Abe-Ouchi, A., Shepherd, A., 2016. Ice sheet model intercomparison project (ISMIP6) contribution to CMIP6. Geosci. Model Dev. Discuss. (GMDD) 1–42, 2016.

Price, S.F., Payne, A.J., Howat, I.M., Smith, B.E., 2011. Committed sea-level rise for the next century from Greenland ice sheet dynamics during the past decade. Proc. Natl. Acad. Sci. Unit. States Am. 108, 8978–8983.

Raymond, C., 1987. How do glaciers surge? A review. J. Geophys. Res. 92, 9121–9134.

Rémy, F., Parouty, S., 2009. Antarctic ice sheet and radar altimetry: a review. Rem. Sens. 1, 1212–1239.

Rignot, E., Mouginot, J., Larsen, C., Gim, Y., Kirchner, D., 2013. Low-frequency radar sounding of temperate ice masses in Southern Alaska. Geophys. Res. Lett. 40, 5399–5405.

Seroussi, H., Nowicki, S., Payne, A.J., Goelzer, H., Lipscomb, W.H., Abe Ouchi, A., Agosta, C., Albrecht, T., Asay-Davis, X., Barthel, A., et al., 2020. Ismip6 Antarctica: a multi-model ensemble of the antarctic ice sheet evolution over the 21st century. Cryosphere Discuss. 14.

Slater, T., Shepherd, A., McMillan, M., Muir, A., Gilbert, L., Hogg, A.E., Konrad, H., Parrinello, T., 2018. A new digital elevation model of Antarctica derived from CryoSat-2 altimetry. Cryosphere 12, 1551–1562.

Sokolov, A., Kicklighter, D., Schlosser, A., Wang, C., Monier, E., Brown-Steiner, B., Prinn, R., Forest, C., Gao, X., Libardoni, A., et al., 2018. Description and Evaluation of the MIT Earth System Model (MESM) manuscript submitted for publication, 5.

Sørensen, L.S., Simonsen, S., Langley, K., Gray, L., Helm, V., Nilsson, J., Stenseng, L., Skourup, H., Forsberg, R., Davidson, M., 2018. Validation of Cryosat-2 SARIn data over Austfonna ice cap using airborne laser scanner measurements. Rem. Sens. 10, 1354.

Stocker, T.F., Qin, H., Plattner, G.-K., Tignor, M., Allen, S.K., Boschung, J., Nauels, A., Xia, Y., Bex, V., Midgley, P.M.e., 2013. Climate Change 2013: the Physical Science Basis. Contribution of Working Group I to the Fifth Assessment Report of the Intergovernmental Panel on Climate Change. Cambridge University Press.

Tangborn, W., 2013. Mass balance, runoff and surges of Bering Glacier, Alaska. Cryosphere 7, 867–875.

Trantow, T., 2014. Numerical Experiments of Dynamical Processes during the 2011-2013 Surge of the Bering-Bagley Glacier System, Using a Full-Stokes Finite Element Model. Master's thesis University of Colorado.

Trantow, T., 2020. Surging in the Bering-Bagley Glacier System, Alaska – Understanding Glacial Acceleration through New Methods in Remote Sensing, Numerical Modeling and Model-Data Comparison. University of Colorado. Ph.D. thesis.

Trantow, T., Herzfeld, U., 2016. Spatiotemporal mapping of a large mountain glacier from CryoSat-2 altimeter data: surface elevation and elevation change of Bering Glacier during surge (2011-2014). Int. J. Rem. Sens. 28.

Trantow, T., Herzfeld, U.C., 2018. Crevasses as indicators of surge dynamics in the Bering Bagley Glacier System, Alaska: numerical experiments and comparison to image data analysis. J. Geophys. Res.: Earth Surf. 123.

Truffer, M., Echelmeyer, K.A., 2003. Of isbrae and ice streams. Ann. Glaciol. 36, 66–72.

Vaughan, G., 1993. Relating the occurrence of crevasses to surface strain rates. J. Glaciol. 39.

Van der Veen, C., 1998. Fracture mechanics approach to penetration of surface crevasses on glaciers. Cold Reg. Sci. Technol. 27, 31–47.

Van der Veen, C., 1999. Crevasses on glaciers 1. Polar Geogr. 23, 213–245.

Voldoire, A., Sanchez-Gomez, E., y Melia, D.S., Decharme, B., Cassou, C., Senesi, S., Valcke, S., Beau, I., Alias, A., Chevallier, M., et al., 2013. The CNRM-CM5. 1 global climate model: description and basic evaluation. Clim. Dynam. 40, 2091–2121.

Wingham, D.J., Francis, C.R., Baker, S., Bouzinac, C., Cullen, R., de Chateau-Thierry, P., Laxon, S.W., Mallow, U., Mavrocordatos, C., Phalippou, L., Ratier, G., Rey, L., Rostan, F., Viau, P., Wallis, D., 2006. CryoSat: a mission to determine the fluctuations in Earth's land and marine ice fields. Adv. Space Res. 841–871.

Winkelmann, R., Martin, M.A., Haseloff, M., Albrecht, T., Bueler, E., Khroulev, C., Levermann, A., 2011. The potsdam parallel ice sheet model (pism-pik)–part 1: model description. Cryosphere 5, 715–726.

Zwally, H.J., Bindschadler, R., Brenner, A., Martin, T., Thomas, R., 1983. Surface elevation contours of Greenland and antarctic ice sheets. J. Geophys. Res.: Oceans 88, 1589–1596.